UNIVERSITAT POLITÈCNICA DE VALÈNCIA

Escuela Técnica Superior de Ingeniería del Diseño

von Kármán Institute for Fluid Dynamics
Aeronautics and Aerospace Department

Heat Capacity Determination of New Lightweight Ablators

Carlos García Guillamón

Supervisor UPV	Laura Contat Rodrigo
Supervisor VKI	Thierry Magin
Advisor VKI	Francisco José Torres Herrador

September 2018

Acknowledgements

This work culminates a six-year period that began when I started my Bachelor of Science at the Universitat Politècnica de València, and which finishes now with this Master Thesis.

Firstly, I would like to thank my supervisor, Pr. Thierry Magin, for his support and guidance during my internship at the VKI. Our meetings and his patience have been fundamental for making me grow as a researcher and engineer. Thanks also to my UPV supervisor, Pr. Laura Contat, for our emails, our meetings and her revisions of this report. Without her help you, reader, would not be reading these lines.

A big thanks to Francisco José Torres Herrador, my advisor at the VKI. Not a single line of this report could have been written without his support and his time. Thanks to him I have learnt more than ever, and I have been able to enjoy research.

Thanks also to Joffrey Coheur and Anabel del Val, from the VKI, for helping me to deal with the black magic of Bayesian inference and Uncertainty Quantification.

I must also remember the people from my Erasmus in Delft: the Squad and the EduP family. Even if each one of us is now in a different country, our five months together were an unforgettable experience and made me enjoy the Netherlands as if it were my own land.

Now, going from the Netherlands to Belgium, I must first thank my landlady Laurence for becoming my belgian mother and making me feel at home during five months. Also thanks to Ilan, her son, for being my belgian brother despite the language differences that made communication between us impossible. And, of course, thanks to my fluffy little friend, my four-legged buddy *Touch*, for his friendship.

Still in Belgium, it is compulsory for me to thank my VKI friends: Claire, Daniel Gabor, Dean, Deniz, Guillermo, Isabel, Javi 123, Hazal, José, Marc, Marco, Mathisse, Richard *Pepino*, Salvatore and Vafakos. In five months we have suffered together at the STP room and at the Computer Center, we have explored Brussels and we have had countless beer-meetings and nights out in Rhode-Saint-Genèse. Thanks also to Pablo Hernando for showing me Gent.

Special thanks to Walter Agostinelli, for being always there to remember the coffee break and the lunch time. And special thanks to Arianna Passaretti, for our conversations, her company and her support.

I must finish this where it began: in Spain. Thanks to my university friends, *Los Mirlos*, for all these years of painful, endless study nights which are already over, but also for their friendship, shared trips and experiences.

Thanks also to my friends from Requena, my home. Thanks to you, every time I go back I feel like if nothing had changed. Despite the kilometers that separate us since I decided to leave Spain, we still grow together and every time we meet we enjoy our time as when we were 16 years old.

Last, but not least, thanks to my whole family. Thanks to my uncle Eloy and to my grandma Nieves for, even though they will never understand my wish of travelling and living in other countries to grow as a person, having a smile every time we see each other. Thanks to my brother Javier, for our deep conversations about everyting imaginable and his pieces of advice about the *Gym*. And finally, thanks to my parents, José and Gloria, for giving me everything they have been able to, for always supporting my choices and encouraging me to continue despite the drawbacks, and for making me the person I am. Thanks to you, I have learnt to fly.

Contents

List of Figures

List of Tables

List of Symbols

Acronyms

0D	Dimensionless Model
DLR	Deutsches Zentrum für Luft- und Raumfahrt
DSC	Differential Scanning Calorimetry
GA	Genetic Algorithm
LCA	Lightweight Ceramic Ablator
LEO	Low Earth Orbit
MSR	Mars Sample Return
MCMC	Markov Chain Monte Carlo
NASA	National Aeronautics ans Space Administration
PDF	Probability Density Function
PICA	Phenolic Impregnated Carbon Ablator
STS	Space Transportation System
TACOT	Theoretical Ablative Composite for Open Testing
TPS	Thermal Protection System
UQ	Uncertainty Quantification
US	United States
USSR	Union of Soviet Socialist Republics
VKI	von Karman Institute for Fluid Dynamics

Greek Symbols

α	$\mathrm{K\,s^{-1}}$	Acceptance probability in bayesian inference
β	$\mathrm{K\,s^{-1}}$	Heating rate
γ		Step in the gradiendt descent algorithm
ϵ		Volume fraction
ζ		Stoichiometric coefficient
$\boldsymbol{\theta}$		Vector containing parameters for Bayesian inference
μ	$\mathrm{Pa\,s}$	Dynamic viscosity
π_j	$\mathrm{kg\,m^{-3}\,s^{-1}}$	Pyrolysis production term for j^{th} gas phase
Π_g	$\mathrm{kg\,m^{-3}\,s^{-1}}$	Global pyrolysis production term for gas phases
ρ	$\mathrm{kg\,m^{-3}}$	Density

ρ_v	$\mathrm{kg\,m^{-3}}$	Virgin material density
σ	$\mathrm{kJ\,kg^{-1}\,K^{-1}}$	Standard deviation
χ	$\mathrm{kJ\,kg^{-1}\,K}$	Advancement of reaction
ω_i	$\mathrm{kg\,m^{-3}\,s^{-1}}$	Pyrolysis production term for i^{th} solid phase
Ω_S	$\mathrm{kg\,m^{-3}\,s^{-1}}$	Global pyrolysis production term for solid phases

Roman Symbols

A	$\mathrm{kJ\,kg^{-1}\,K^{-1}}$	Pre-exponential factor for Arrhenius expression
c_p	$\mathrm{kJ\,kg^{-1}\,K^{-1}}$	Specific heat capacity
$c_{\mathrm{p_{Apparent}}}$	$\mathrm{kJ\,kg^{-1}\,K^{-1}}$	Apparent specific heat capacity
$c_{\mathrm{p_{Baseline}}}$	$\mathrm{kJ\,kg^{-1}\,K^{-1}}$	Baseline specific heat capacity
$c_{\mathrm{p_{DSC_i}}}$	$\mathrm{kJ\,kg^{-1}\,K^{-1}}$	Experimental $c_{\mathrm{p_{Apparent}}}$ at datapoint i
$c_{\mathrm{p_{PATO_i}}}$	$\mathrm{kJ\,kg^{-1}\,K^{-1}}$	Numerical $c_{\mathrm{p_{Apparent}}}$ at datapoint i
E	$\mathrm{J\,mol^{-1}}$	Activation energy
F		Fraction of density loss
$F\left(\boldsymbol{X}\right)$		Objective function for optimization
$\mathcal{F}_j$		Effective diffusion flux of gas phase j
h	$\mathrm{kJ\,kg^{-1}}$	Enthalpy
h_0	$\mathrm{kJ\,kg^{-1}}$	Total enthalpy
h_∞	$\mathrm{kJ\,kg^{-1}}$	Static enthalpy of the farfield flow
Δh^0	$\mathrm{kJ\,kg^{-1}}$	Enthalpy of formation
Δh_pyro	$\mathrm{kJ\,kg^{-1}}$	Enthalpy released/absorbed during pyrolysis reaction
J		Fitness function
k		Rate of reaction
$\boldsymbol{K}$	$\mathrm{m^2}$	Permeability tensor
$\dot{m}$	$\mathrm{kg\,s^{-1}}$	Mass flow
m	kg	Mass
m_0	kg	Mass before pyrolysis reaction
m_∞	kg	Mass after pyrolysis reaction
$\mathcal{M}_j$		Mole fraction of gas phase j
n		Arrhenius parameter
N_g		Number of gas phases resulting from pyrolysis
N_p		Number of solid phases undergoing pyrolysis
N_var		Number of optimization variables
n		Arrhenius parameter

p		Probability distribution function
q		Proposal distribution function in Bayesian inference
r		Acceptance ratio
M		Mach number
R	$\mathrm{J\,mol^{-1}\,K^{-1}}$	Universal gas constant
t	s	Time
T	K	Temperature
u_∞	$\mathrm{m\,s^{-1}}$	Speed of the farfield flow
$\boldsymbol{v_g}$	$\mathrm{m\,s^{-1}}$	Convective velocity of gas
V	V	Voltage obtained from DSC experiments
y_j		Mass fraction of gas phase j
$\boldsymbol{y}$		Vector containing observed data for Bayesian inference
$\boldsymbol{X}$		Vector containing optimization design variables

Subscripts

0	Initial conditions
∞	Ambient
g	Gas phases
i	i$^{\mathrm{t}}$h datapoint
i	i^{th} solid phase
j	j^{th} gas phase
k	k^{th} iteration in algorithm
pyro	Constants belonging to the kinetic model for pyrolysis
s	Solid phases

Superscripts

0	Standard conditions
blank	Data obtained from blank run in DSC experiments
medium	Medium data obtained in Uncertainty Quantification
reference	Reference material for DSC experiments
sapphire	Sapphire material

Chapter 1
Introduction

In his novel *From the Earth to the Moon*, published in 1865, Jules Verne deals with space travel and depicts an early concept of space exploration from the point of view of science fiction. He could not imagine at the time, nevertheless, the strong influence that his novel would have in the conquer of the space. His novel would inspire figures of the XX century as important as Konstantin Tsiolkovsky, father of the well-known rocket equation; Hermann Oberth, german rocketry pioneer; and Wernher von Braun, german aerospace engineer who designed the rocket Saturn V which would take the spacecrafts of the Apollo program. It was von Braun's rocket which, in 1969, would take the crew of the Apollo 11 to the Moon, hence making true the trip that Verne imagined in 1865.

The XX century was a key age for the development of astronautics. The ideas of Tsiolkovsky, Oberth and Robert Goddard, considered as the fathers of astronautics, were put into practice for the development of the first rockets. It would not be until the Cold War between the Soviet Union (USSR) and the United States (US), held from the middle of the 40's until the beginning of the 90's, when astronautics would see a considerable boost. Both rivals competed for the conquer of space and the development of spaceflight. This space competence was triggered in 1957, when the USSR launched the first satellite into space, the Sputnik 1: this event started the Space Race, which would last until the USSR dissolution in 1991. Important milestones of the Space Race include the launch of the first human into space, the soviet Yuri Gagarin, on board of the Vostok spaceship in 1961 (Figure 1.1 left); and the arrival of the first humans to the Moon, achieved in 1969 by the US with the Apollo 11 spaceship (Figure 1.1 right).

Figure 1.1: Left: Soyuz rocket containing the Vostok 1 spaceship [36]. Right: Launch of the Saturn V rocket containing the Apollo 11 spaceship [19].

In a space exploration mission, a payload is taken to space in order to achieve a purpose. This payload can be a spaceship with manned crew inside, a satellite, an interplanetary probe, etc. In any case, a space exploration mission consists of different phases. The first step to reach the space is the launch phase, in which the spacecraft is placed inside a rocket which will provide the necessary thrust force to overcome Earth's gravity and reach outer space. Then, depending on the extent of the mission, different phases can be distinguished. In most missions the payload will need to go back to Earth or to enter another planet's atmosphere. When the vehicle enters into contact with an atmosphere when coming back from outer space, high heat fluxes appear and transfer energy from the flowfield to the spacecraft. This phase is addressed as re-entry when the spacecraft is coming back to Earth, and entry when it is entering into a different celestial body.

Re-entry is one of the most crucial phases of a space mission. During re-entry the vehicle is traveling at a high speed u_∞. Figure 1.2 shows typical values for Earth re-entry speeds: for Low Earth Orbit (LEO) missions like the Space Shuttle, u_∞ is of the order of 8 km/s; for missions coming back from Mars, u_∞ can take values larger than 15 km/s. Figure 1.2 also shows physico-chemical phenomena associated with high-speed flight.

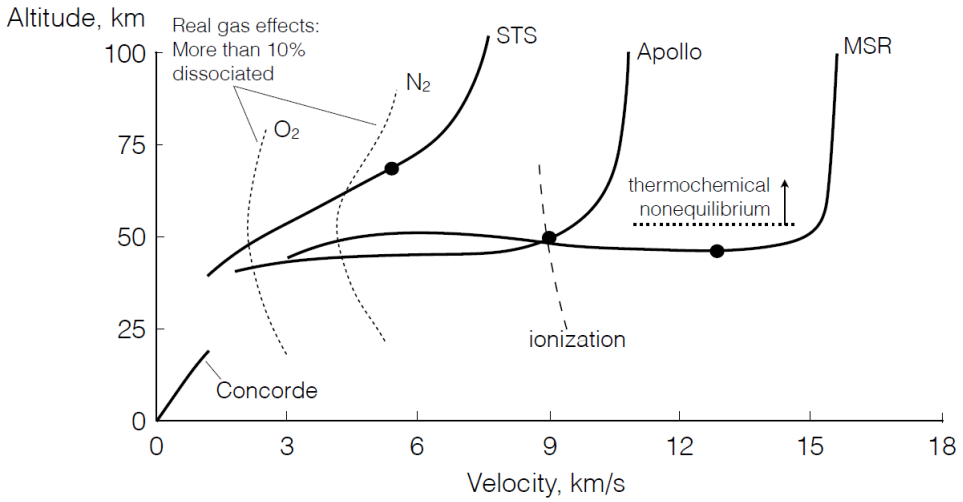

Figure 1.2: Flight envelope (altitude versus speed) for different re-entry missions: Space Shuttle (STS), Apollo and Mars Sample Return (MSR) [12]. The point of maximum heat flux is shown by the bullet point. The Concorde envelope is shown for comparison.

The high re-entry speed yields a total enthalpy h_0 according to the following expression:

$$h_0 = h_\infty + \frac{1}{2}u_\infty^2 \tag{1.1}$$

Where h_∞ are $\frac{1}{2}u_\infty^2$ are the static enthalpy and the kinetic energy per unit mass, respectively. In the re-entry context, the static enthalpy is negligible compared to the kinetic energy. This total enthalpy is a measure of the energy associated to re-entry. During the descent trajectory, this energy is dissipated into heat. The re-entry vehicles usually present a blunt shape because, according to blunt body theory [3], this is the optimal shape to dissipate heat into the atmosphere instead of transferring heat to the vehicle. When re-entering the atmosphere, a detached bow shock is formed at the nose of the vehicle. A typical blunt body and the bow shock can be appreciated in Figure 1.3.

The air is strongly compressed at the bow shock. Temperature rises up to 10 000 K, and real gas effects take place. Downstream of the bowshock heat is dissipated into the atmosphere and the flow temperature decreases. The temperature at the nose of the vehicle depends on the re-entry speed, but usual values can oscillate between 1000 K and 3000 K [3].

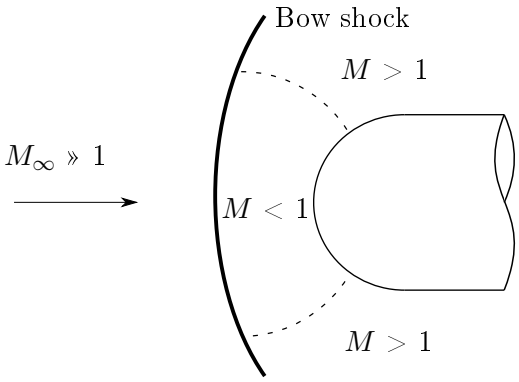

Figure 1.3: Hypersonic scenario: schematic drawing of a bow shock around blunt body. Dash line is the sonic line, i.e. the line in which the Mach number is 1.

The need of protecting the vehicle stems from the high temperatures encountered at the nose of the vehicle. This is the task of the **Thermal Protection Systems** (**TPS**). Not many materials can cope with such high temperatures: most of them melt before 2000 K, and only some metals can withstand temperatures close to 3000 K.

TPS, also known as heat shields, can be classified in two groups [12]:

- **Reusable**. Composed mainly of ceramic tiles, made of materials such as silica (SiO_2) and alumina (Al_2O_3). This type of heat shield can be used more than once. They can be used for re-entry speeds up to 8 km/s: larger speeds would increase the temperatures to values beyond the melting point of the ceramic tiles. The main mechanism by which the reusable TPS protect the spacecraft is known as catalysis, a gas-surface interaction phenomenom. The gas atoms reaching the surface of the TPS use the latter as a catalyst to recombine, releasing energy which is partially stored in the surface [4]. A spacecraft using reusable TPS is the Space Shuttle. A ceramic tile can be seen in Figure 1.4 left.

- **Ablative**. Composite materials, called ablators, are used. Ablators are made of fibers (glass of carbon) joined by a resin (usually phenol). They degrade and lose mass when absorbing heat. This heat shield can only be used once, but can withstand larger speeds than the reusables ($u_\infty > 8$ km/s). There are no materials that can cope with the high temperatures associated to these speeds (3000 K), so heat shields made of ablative materials that decompose are the only ones that can be used under these conditions. Soyuz uses this type of TPS (Figure 1.4 right).

The **ablative TPS** was firstly defined by Robert H. Goddard in 1920. In his *Report Concerning Further Developments* [10], he proposed a way to return to Earth by covering the spacecraft with "layers of a very infusible hard substance with layers of a poor heat conductor between". This idea was inspired by the entry of meteors in Earth, as they degrade following this mechanism. The first vehicle that used ablative TPS was the Mark 3 re-entry vehicle, in 1959 [7]. It was shielded by a composite made of phenolic resin with pieces of nylon cloth. Thanks to this ablative heat shield, the weight of the Mark 3 was almost 600 kg lighter than its predecessor Mark 2, which used an old type of TPS based on metallic materials called heat sink. This type of TPS was used in the first re-entry vehicles, before ablators appeared. Ablative heat shields were also used in the Apollo 11 in 1969, to bring back the crew from the Moon to the Earth. In this case the material used was a stainless steel honeycomb with an outer layer of phenolic epoxy resin.

Figure 1.4: Left: Space Shuttle ceramic tile [29]. Right: Soyuz capsule after re-entry [12].

Reusable TPS came after the ablative heat shields. They were used by the first time for the Space Shuttle in 1981. Their main disadvantage is their re-entry speed limit to 8 km/s. Future missions intend to reach other planets, such as Mars, where the re-entry speeds are considerably faster than 8 km/s. Reusable TPS cannot be used for those missions. Instead, **ablative heat shields** are widely used due to its wide application range: they can be used from low re-entry speeds (Dragon spacecraft by SpaceX, with a re-entry speed of 7.6 km/s) until very high ones (Mars Sample Return, with a re-entry speed of 15 km/s). They were used in the fastest re-entry ever achieved, which was performed by the Galileo in 1995 when entering Jupiter. The probe achieved a record entry speed of 48 km/s.

The Galileo probe re-entry, however, made the engineers realise of the uncertainties in the design of TPS. During the design phase it was thought that the center of the heat shield would suffer more heating than the edges, as this is where the stagnation point (maximum heat flux point [18]) is located. Therefore, more material was added in the center than in the edges (Figure 1.5 left). After the entry phase, however, it was found that this did not happen: the material recession was almost uniform along the heat shield. At the center there was less material removed than predicted, and the opposite happened at the edges (Figure 1.5 right). This made the scientific community to realise about lack of accurate tools for the proper TPS design, and the need of improving them.

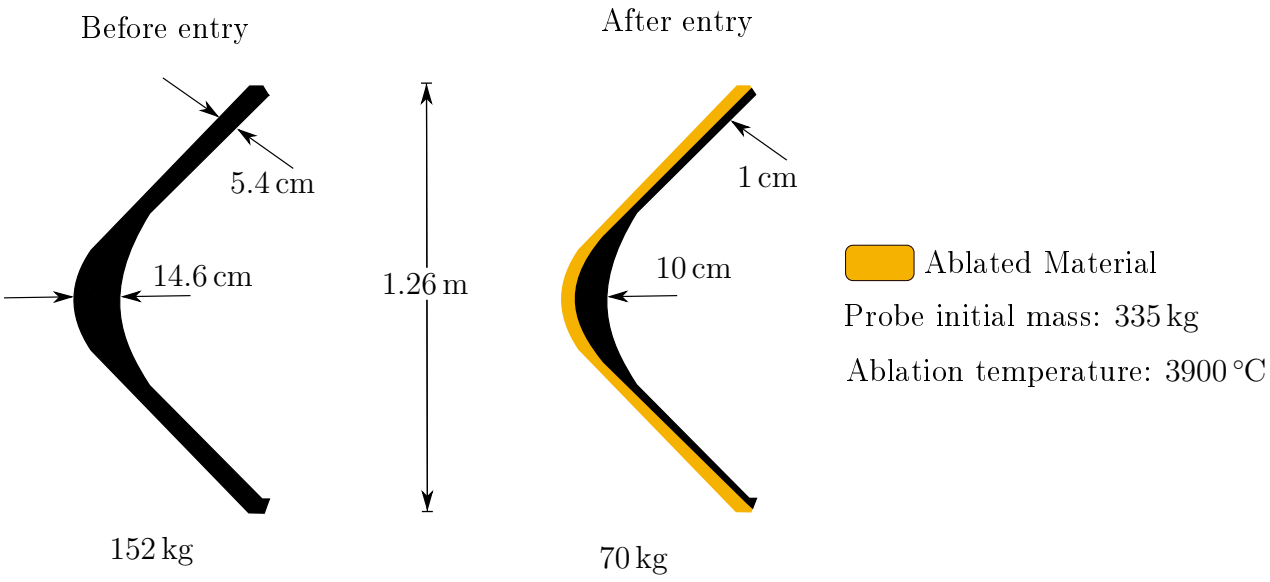

Figure 1.5: Galileo probe before (left) and after (right) entry in Jupiter [17]

The proper design of TPS is also relevant in economic terms. The cost of sending a kilogram of mass to space can amount to 10 000 € for LEO missions [25], and the TPS can suppose up to the 50 % of the total vehicle mass [9] (Figure 1.5). By improving the design of the TPS the weight of the spacecraft can be minimized, and the cost of the mission would decrease.

The scenario found by ablative heat shields during re-entry is shown in Figure 1.6. The bow shock, the temperatures reached and the real gas effects are shown. For re-entry into the Earth atmosphere, composed mainly of N_2 and O_2 molecules, real gas effects include dissociation (diatomic molecules react and become monoatomic elements) and ionization (monoatomic elements react and release free electrons). Typical dissociation reactions are given by (1.2). The ionization between dissociated O_2 and N_2 is expressed by (1.3)

$$O_2 \rightleftharpoons 2\,O \qquad N_2 \rightleftharpoons 2\,N \tag{1.2}$$

$$N + O \rightleftharpoons NO^+ + e^- \tag{1.3}$$

After ionisation the flow is in plasma state. Plasma differs from gas state in the fact that the particles are electrically charged. The plasma flow radiates a considerable amount of heat to the atmosphere, and when it reaches the boundary layer, the temperature has decreased by several thousands of degrees, e.g. 6000 K.

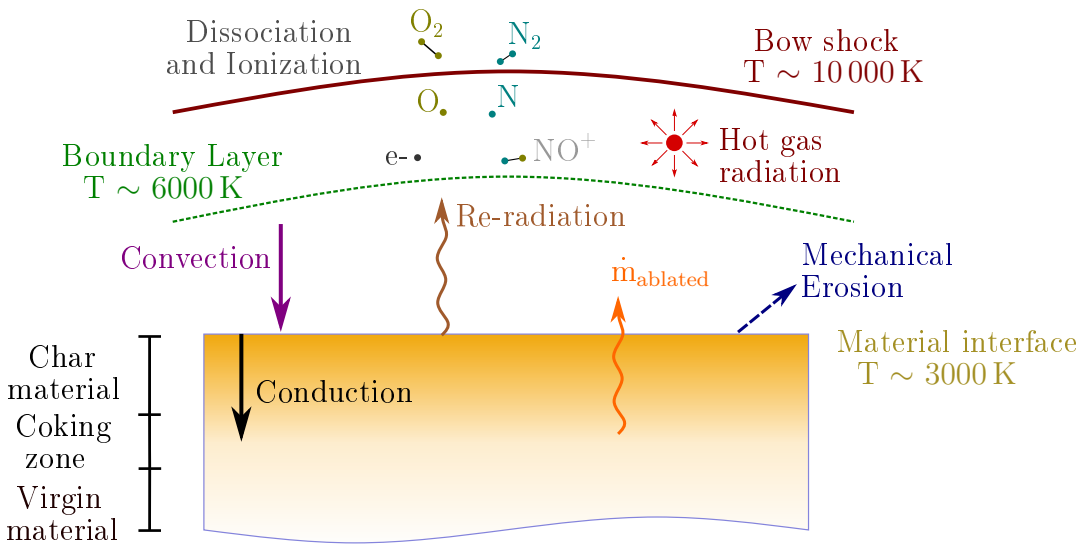

Figure 1.6: Coupled physics-chemistry phenomena in an ablative material during re-entry.

Inside the boundary layer, heat is transferred by convection from the hot flow to the interface of the material. Then, heat transfer by conduction occurs inside the material. The material degrades due to the high temperature following two mechanisms:

- **Pyrolysis**. Due to the high temperatures, the resin decomposes and becomes a low-density char. Around 50 % of the mass is lost due to vaporization, which produces pyrolysis gases. These gases are then blown to the atmosphere [12]. It is an endothermic process, as it consumes energy.
- **Ablation**. After pyrolysis, resin has become char. What is left then is the charred resin and the carbon fibers. This material is ablated in different ways: it can react with the monoatomic carbon and oxygen to form molecules (chemical ablation), as shown in (1.4);

it can sublimate due to the high temperatures; or it can be removed by mechanical erosion due to internal stresses, also known as spallation.

$$C + O \rightleftharpoons CO \qquad C + N \rightleftharpoons CN \tag{1.4}$$

In Figure 1.6, $\dot{m}_{ablated}$ represents the pyrolysis gases and the ablation due to chemistry and sublimation. The high temperatures yield re-radiation from the material outwards to the atmosphere. The pyrolysis gases which are transported outwards also absorb heat, decreasing the amount of heat transferred to the interface of the material by convection: this is known as blowing [12]. Thanks to re-radiation, spallation and blowing, temperature is reduced from 6000 K in the boundary layer to 3000 K at the interface of the material.

Depending on the degree of material degradation, three sections can be distinguished in the heat shield (Figure 1.6):

- **Virgin material**. Original material of the ablator before the re-entry, i.e. before the material has not undergone any pyrolysis reactions. The virgin material is composed of carbon fibers and phenolic resin.
- **Char material**. Region of the TPS which has undergone pyrolysis reactions. The char material is composed of carbon: carbon fibers and carbonized resin.
- **Coking zone**. Intermediate zone in which virgin and char material are found in different compositions. Pyrolysis reactions take place in this region.

Recent advances in ablative TPS have led to the development of a new series of composite materials called **Lightweight Ceramic Ablators** (**LCA**). These materials are composed of carbon fibers (C) impregnated with a phenolic resin (C_6H_6O). They present a large porosity (80 to 90 %), low density (200 - 300 kg/m^3) [32] and low conductivity [33], hence reducing weight. Furthermore, they are able to absorb a big amount of heat thanks to the endothermic pyrolysis reactions. These two features make them suitable as ablative materials. Some examples of LCAs are PICA, developed by National Aeronautics and Space Administration (NASA) and used in Stardust (2006) and Mars Science Laboratory (2012) missions; Asterm, developed by Airbus; and Zuram , developed by the German Aerospace Center (DLR). Ablative LCAs can be seen in Figure 1.7.

Figure 1.7: Left: Mars Science Laboratory PICA heat shield [12]. Right: Zuram sample [31]

Micrographies of virgin and charred PICA are shown in Figure 1.8. The virgin PICA sample shows the phenolic resin bonding the carbon fibers. The charred sample shows the burnt fibers and the charred resin. The mass loss due to the decomposition of the resin is noticed.

Despite the success of the Stardust and Mars Science Laboratory missions, the proper design of LCA type heat shields has some limitations. This is because some properties of these materials, such as the specific heat capacity at constant pressure c_p and the enthalpy h, are uncertain, as

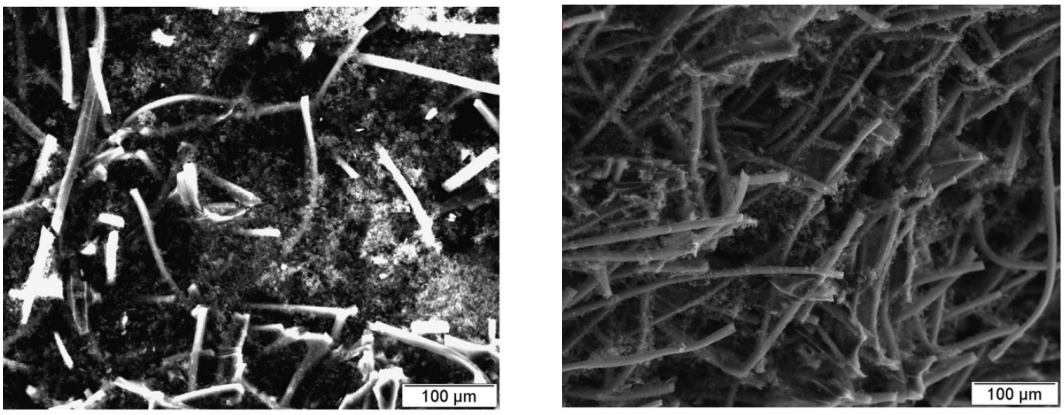

Figure 1.8: Micrography of PICA. Left: virgin sample. Right: charred sample [35].

they are difficult to obtain from experiments. The reason of these uncertainties arise when performing experimental measurements, as the results have contributions both from physics and chemistry: pyrolysis reactions take place and contaminate the measurements.

The coupling between physics and chemistry is illustrated in Figure 1.9. The blue solid line shows a typical c_p curve that increases with increasing temperature. This is the baseline heat capacity, and it is the expected result from thermodynamics. However, when performing the experiments, the measured curve follows the shape of the black line. The curve is not smooth anymore, but presents a hump that deviates from the baseline c_p. In the region where the hump is present a pyrolysis reaction is taking place. This reaction is endothermic: it is absorbing energy, so the experimental facility needs to increase the heat provided to the material for increasing the temperature, hence increasing the resulting measured heat capacity. This measured heat capacity, given by the black line, is also referred as **apparent heat capacity** [27]. The area between the black and blue lines correspond to the **enthalpy of the pyrolysis reaction**, Δh_pyro. There is the need, therefore, of improving the current techniques and tools used to determine the baseline c_p and, from it, the enthalpy.

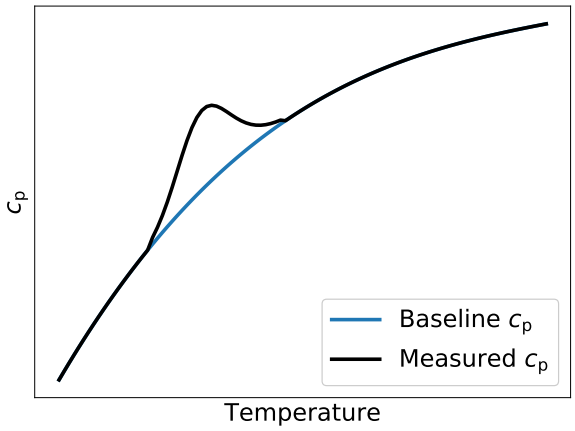

Figure 1.9: Baseline and measured heat capacities.

The aim of this project is to develop an *ad hoc* numerical tool for modelling the thermal characterization of LCA from experimental data. The tool combines a pyrolysis solver based on OpenFOAM with an optimization software. In particular, the tool is developed to be applied to

obtain the heat capacity and the enthalpies of ablative materials. It will also be applied to test cases whose properties are known for code verification.

This report is structured as follows:

- **Chapter 2** - *Materials and Methods*. The materials studied in this project are initially presented. The Differential Scanning Calorimetry technique that is used to obtain c_p experimentally is shown. The equations modelling pyrolysis and the optimization algorithms that are used for numerical c_p determination are introduced. The fitness function used to compare numerical and experimental results is shown, and finally an introduction on Bayesian Inference closes the chapter.
- **Chapter 3** - *Numerical Tool for c_p Determination of Ablative Materials*. The numerical methodology followed to fit c_p to experimental data is described. Pyrolysis solver PATO and optimization toolbox Dakota are introduced. Then, test cases for graphite and TACOT ablative material used for validation of this numerical code are analysed.
- **Chapter 4** - *Conclusions*. Conclusions regarding the implementation of this numerical code for both graphite and TACOT are given.
- **Chapter 5** - *Budget*. The cost of the project is given in this chapter.

Chapter 2
Materials and Methods

2.1 Materials

Two materials have been studied in this project: graphite and TACOT.

Graphite is a material composed solely of carbon. It is usually used as a reference material for code verification, since it does not undergo pyrolysis and its c_p is known. It has been chosen as a first step for c_p determination due to its easier modelling compared to ablative materials.

Theoretical Ablative Composite for Open Testing (**TACOT**) is the ablative material chosen to be studied. It is a theoretical material created by Lachaud et al. [16] for code verification and testing. Its properties are defined based on the mechanical and chemical properties of real ablators, undergoing pyrolysis.

2.2 Experimental Determination of c_p by Differential Scanning Calorimetry

The heat capacity of ablative materials can be determined experimentally using Differential Scanning Calorimetry (DSC). The DSC device consists of a furnace which contains two crucibles (Figure 2.1). Temperature inside the furnace is increased by defining the heating rate β:

$$\beta = \frac{\partial T}{\partial t} \tag{2.1}$$

The crucibles are placed on top of a balance. Each one of them contains a thermocouple that measures their individual temperature. Furthermore, each crucible contains an individual heater. One of the crucibles contains the sample which wants to be tested. The other crucible contains a reference material whose properties are known. Due to the small diameter of the crucibles, the hypothesis of uniform temperature inside them can be assumed [2, 31]. This assumption will considerably simplify subsequent computational analysis.

DSC measures heat flux with respect to time (or temperature). When the temperature increases, the DSC provides a voltage which is proportional to the heat flux absorbed (or released) by the sample. DSC uses the principle of null balance of temperature [26], which consists on keeping the temperature inside the crucibles equal:

$$T^{\mathrm{sample}} - T^{\mathrm{reference}} = 0 \tag{2.2}$$

where T^{sample} is the temperature inside the sample material crucible, and $T^{\mathrm{reference}}$ is the temperature inside the reference material crucible.

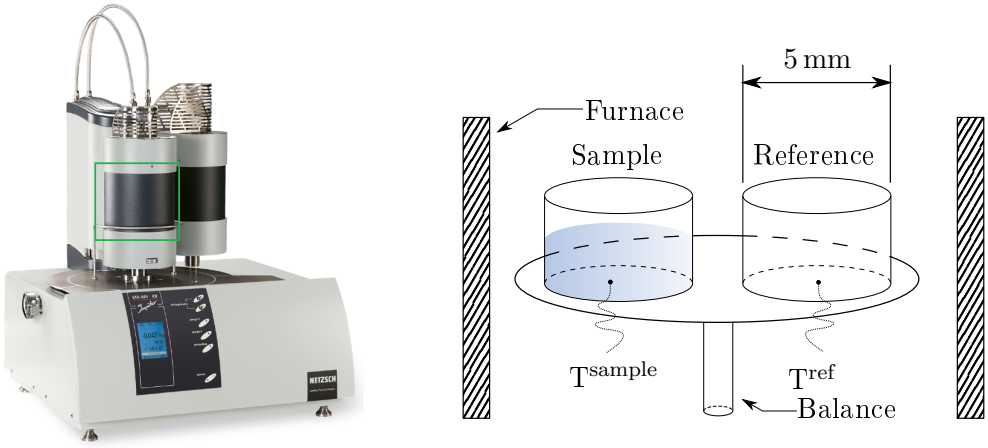

Figure 2.1: Left: NETZSCH 449 F3 Jupiter Simultaneous Thermal Analyser available at the VKI [32]. Right: magnified view of the inside of the furnace in the green rectangle.

A schematic of the DSC is shown in Figure 2.2. Two control loops can be distinguished:

- **Average temperature control loop**. The average temperature inside the furnace is increased according to the defined heating rate. Then, the temperatures of the sample and reference crucibles increase at the same rate.
- **Differential temperature control loop**. The temperatures inside each crucible are monitored with thermocouples. If endothermic or exothermic reactions take place inside the crucibles, T^{sample} and $T^{\text{reference}}$ are different and the principle of null balance is not fulfilled anymore. Individual heaters inside each crucible provide power to maintain the principle of null balance.

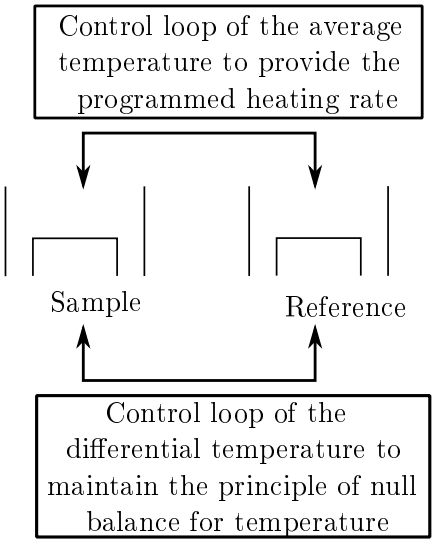

Figure 2.2: DSC crucibles showing control loops [26].

The results from the DSC measurements do not provide the heat capacity straightforward, but a signal which needs to be processed. Different methods can be used to process this signal and obtain the heat capacity from it. A common, standardised one is the sapphire method.

Sapphire Method

In this method, sapphire is used as the reference material. Sapphire is a material with a known heat capacity and which does not undergo any pyrolysis reaction [32].

The sapphire method for determining heat capacity [13] needs three measurements :

1. **Blank run**. Measurement performed without samples inside the crucibles to obtain the heat absorbed by them. From this run the voltage V^{blank} is obtained.
2. **Reference run**. Measurement performed only with sapphire to obtain the heat absorbed by this reference material. From this run the voltage V^{sapphire} is obtained.
3. **Sample run**. The sample is placed into the corresponding crucible and one measurement is performed. From this run the voltage V^{sample} is obtained.

Once the three runs are performed, the voltages obtained are plugged into the following equation to obtain $c_{\text{p}}^{\text{sample}}$:

$$c_{\text{p}}^{\text{sample}} = \frac{m^{\text{sapphire}} \left(V^{\text{sample}} - V^{\text{blank}} \right)}{m^{\text{sample}} \left(V^{\text{sapphire}} - V^{\text{blank}} \right)} c_{\text{p}}^{\text{sapphire}} \tag{2.3}$$

where the heat capacity of sapphire, $c_{\text{p}}^{\text{sapphire}}$, is known from literature [8]; m^{sapphire} is the instantaneous mass of the sapphire (reference) material, and m^{sample} is the instantaneous mass of the sample material.

Dummy Data

In this work, experimental c_{p} data of graphite and TACOT have been modelled instead of being directly measured by DSC. In particular, dummy data, that simulate c_{p} data from DSC experiments, have been generated using the information available in the literature for these reference materials.

The c_{p} of graphite is given in the literature by an analytical function $c_{\text{p}}(T)$ that yields a smooth curve [22]. Dummy data for graphite are then generated by adding a noisy signal to this curve.

On the other hand, the baseline c_{p} for TACOT can be obtained from tabulated data as a function of temperature, available in code libraries [16]. As TACOT is a theoretical material undergoing pyrolysis, dummy data must represent its apparent c_{p}. This apparent c_{p} can be determined with some of the available pyrolysis solvers [14].

2.3 Numerical Determination of c_{p} by Pyrolysis Modelling

Apparent c_{p} determination of ablative materials can also be achieved by means of numerical methods applied to the equations that model pyrolysis [15]. Pyrolisis is one of the most important phenomena associated with thermal decomposition of ablative materials. In this section, the general equations governing pyrolysis are first introduced. Then, a more simplified version of these equations that will be implemented in this work is described. Finally modelling of the material properties, that are needed as input to obtain numerically the apparent c_{p}, is stated.

2.3.1 Governing Equations of Pyrolysis

Kinetic model

The pyrolysis mechanism is described by the pyrolysis model. During pyrolysis a solid phase i decomposes into a gas phase k through a pyrolysis reaction. Mass is lost in this process. Denoting

by $m_{0,i}$ as the initial mass of solid phase i before pyrolysis and $m_{\infty,i}$ as the final mass of the solid phase i after pyrolysis, the **advancement of reaction** χ_i is given by the following expression:

$$\chi_i(t) = \frac{m_{0,i} - m_i(t)}{m_{0,i} - m_{\infty,i}} \tag{2.4}$$

Where $m_i(t)$ is the mass of solid phase i at a given time t.

$m_i(t)$ is bounded by $m_{0,i}$ and $m_{\infty,i}$:

- At $t = 0$, $m_i(t = 0) = m_{0,i}$ and $\chi_i(t = 0) = 0$: the reaction has not started.
- As $t \to \infty$, $m_i(t \to \infty) = m_{\infty,i}$ and $\chi_i(t \to \infty) = 1$: the reaction has finished.

The reactions taking place in pyrolysis can be considered to be heterogeneous. A reaction is heterogeneous when its reactants are components of two or more phases. Pyrolysis can be considered a heterogeneous reaction, as these are solid and gaseous phases. These reactions can be modelled by means of the Arrhenius equation, which defines a rate of the reaction depending on temperature, $k(T)$. The Arrhenius equation is expressed as follows:

$$k_i(T) = A_i \exp\left(-\frac{E_i}{RT_i}\right) \tag{2.5}$$

where A_i is a pre-exponential factor, E_i the activation energy, R is the universal gas constant, and T_i is the absolute temperature. All the magnitudes are referred to a given solid phase i.

The degradation process can be modelled by combining equations (2.4) and (2.5) in the following **kinetic model**:

$$\frac{d\chi_i}{dt} = f(\chi_i)\, k(T) = f(\chi_i)\, A_i \exp\left(-\frac{E_i}{RT_i}\right) \tag{2.6}$$

where the function $f(\chi_i)$ depends on the mechanism of degradation. This expression is widely accepted as a general model to represent the degradation of materials [31, 32, 34].

Equation (2.6) can model different mechanisms of thermal decomposition by changing the expression for $f(\chi_i)$. These mechanisms depend on materials properties such as the microstructure and the density. Some examples of these expressions are shown in Table 2.1.

Table 2.1: Mechanisms of thermal decomposition [31]

Kinetic model	$\boldsymbol{f(\chi_i)}$
Nucleation and Grow	$1/n_i\,(1-\chi_i)\left(-\ln(1-\chi_i)\right)^{\frac{n_i-1}{n_i}}$
Phase boundary reaction	$n_i\,(1-\chi_i)^{\frac{n_i-1}{n_i}}$
Diffusion	$1/\chi_i$
Power law	$\left(1/n_i\right)\chi_i^{1-n_i}$
Chemical reaction	$(1-\chi_i)^{n_i}$

By paying attention to Equation 2.6 and the expressions for $f(\chi_i)$, it can be seen that there are three constants which play an important role in the degradation model: E_i, A_i and n_i. This combination of constants is known as the kinetic triplet.

As a solid phase i changes to gaseous state, density of the material decreases. There are several models used to represent this **density loss**. The most common one represents the density as a function of the advancement of reaction by means of the following model:

$$\rho(t) = \rho_v \sum_{i=1}^{N_p} F_i \chi_i(t) \tag{2.7}$$

where ρ_v is the density of the virgin material, F_i is the fraction of density loss at the i^{th} reaction and N_p is the number of solid phases undergoing pyrolysis reactions.

Solid phase mass conservation

For representing the decomposition of a solid phase it is useful to introduce the pyrolysis production term ω_i, given by:

$$\omega_i = \epsilon_{0,i}\rho_{0,i}F_i\frac{d\chi_i}{dt} \tag{2.8}$$

where $\epsilon_{0,i}$ and $\rho_{0,i}$ are the volume fraction and density of the solid phase i at the initial time.

The mass conservation equation applied to a solid phase i from a solid body composed by N_p solid phases is given as follows:

$$\underbrace{\frac{\partial(\epsilon_i\rho_i)}{\partial t}}_{\substack{\text{Accumulation}\\ \text{term}}} = -\underbrace{\omega_i}_{\substack{\text{Pyrolysis}\\ \text{production}}} = -\epsilon_{0,i}\rho_{0,i}F_i\frac{d\chi_i}{dt} \qquad \forall i \in N_p \tag{2.9}$$

Adding all the solid constituents N_p, a global solid mass balance can be obtained:

$$\underbrace{\frac{\partial(\epsilon_s\rho_s)}{\partial t}}_{\substack{\text{Accumulation}\\ \text{term}}} = -\underbrace{\Omega_s}_{\substack{\text{Pyrolysis}\\ \text{production}}} = -\sum_{i=1}^{N_p}\omega_i \tag{2.10}$$

where Ω_s represents the total mass change rate of the solid due to heterogeneous reactions.

Gas phase mass conservation

The global mass conservation equation applied to a gas phase j from a vapour composed by N_g gas species is given by:

$$\underbrace{\frac{\partial(\epsilon_\mathrm{g}\rho_\mathrm{g})}{\partial t}}_{\substack{\text{Accumulation}\\ \text{term}}} + \underbrace{\frac{\partial(\epsilon_\mathrm{g}\rho_\mathrm{g}\boldsymbol{v_\mathrm{g}})}{\partial \boldsymbol{x}}}_{\substack{\text{Convective}\\ \text{term}}} = \underbrace{-\sum_{j=1}^{N_\mathrm{g}}\frac{\partial(\epsilon_j\rho_j)}{\partial t}}_{\substack{\text{Pyrolysis-gas}\\ \text{production}}} \tag{2.11}$$

where ϵ_g, ρ_g and $\boldsymbol{v_\mathrm{g}}$ are the volume fraction, the density and the convective velocity of the gas respectively. ϵ_j and ρ_j are the volume fraction and density of the gas species j. Equilibrium chemistry is assumed. Bold symbol indicates vectorial magnitude.

In order to account for the volatiles production due to the decomposition of the solid phase, the production rate of gas species j is given by π_j:

$$\pi_j = \sum_{i=1}^{N_\mathrm{p}}\zeta_{j,i}\omega_i \tag{2.12}$$

Where $\zeta_{j,i}$ is a stoichiometric coefficient. The term π_j can be summed over all the gas species to yield the overall pyrolysis-gas production rate Π_g, which is equal to the right hand side of (2.11):

$$\Pi_{\mathrm{g}} = \sum_{j=1}^{N_{\mathrm{g}}} \pi_j = \sum_{j=1}^{N_{\mathrm{g}}} \frac{\partial \left(\epsilon_j \rho_j\right)}{\partial t} \tag{2.13}$$

Considering that all the N_{p} solid phases undergo pyrolysis reactions to form N_{g} gaseous species, the overall pyrolysis-gas production must be equal to the total mass change rate of the solid phases:

$$\Pi_{\mathrm{g}} = \Omega_{\mathrm{s}} \tag{2.14}$$

Hence, the global mass conservation of the gas species can be also expressed as:

$$\underbrace{\frac{\partial \left(\epsilon_g \rho_g\right)}{\partial t}}_{\substack{\text{Accumulation} \\ \text{term}}} + \underbrace{\frac{\partial \left(\epsilon_g \rho_g \boldsymbol{v_g}\right)}{\partial \boldsymbol{x}}}_{\substack{\text{Convective} \\ \text{term}}} = \underbrace{-\sum_{j=1}^{N_g} \frac{\partial \left(\epsilon_j \rho_j\right)}{\partial t}}_{\substack{\text{pyrolysis} \\ \text{production}}} = \Pi_g = \Omega_s \tag{2.15}$$

Species conservation

The conservation equation for species mass fraction y_j is:

$$\underbrace{\frac{\partial \left(\epsilon_{\mathrm{g}} \rho_{\mathrm{g}} y_j\right)}{\partial t}}_{\substack{\text{Accumulation} \\ \text{term}}} + \underbrace{\frac{\partial \left(\epsilon_{\mathrm{g}} \rho_{\mathrm{g}} y_j \boldsymbol{v_g}\right)}{\partial \boldsymbol{x}}}_{\substack{\text{Advection} \\ \text{term}}} + \underbrace{\frac{\partial \mathcal{F}_j}{\partial \boldsymbol{x}}}_{\substack{\text{Diffusion} \\ \text{term}}} = \pi_j + \underbrace{\epsilon_{\mathrm{g}} \omega_j \mathcal{M}_j}_{\substack{\text{Chemical} \\ \text{species production}}} \qquad \forall j \in N_{\mathrm{g}} \tag{2.16}$$

where y_j and $\mathcal{M}_j$ are the mass and mole fractions of gas species j respectively, and $\mathcal{F}_j$ is the effective diffusion flux, given by the Fick's first law. The advection and diffusion terms combined represent the convection.

Momentum conservation

The momentum conservation equation for porous media is given by:

$$\boldsymbol{v_g} = -\frac{1}{\epsilon_{\mathrm{g}}} \left(\frac{1}{\mu} \underline{\underline{\boldsymbol{K}}} + \frac{1}{p} \underline{\underline{\beta}} \right) \cdot \frac{\partial p}{\partial \boldsymbol{x}} \tag{2.17}$$

where $\underline{\underline{\boldsymbol{K}}}$ is the permeability tensor, μ is the viscosity, p is the pressure and β is the Klinkenberg correction to account for slip effects.

Energy conservation

The derivation for the energy equation can be found in [31] and, in a more general way, in [15]. Here the final shape of the energy equation is shown, given by the following expression:

$$\begin{aligned} &\overbrace{\frac{\partial \left(\epsilon_{\mathrm{g}} \rho_{\mathrm{g}} h_{\mathrm{g}} - \epsilon_{\mathrm{g}} p\right)}{\partial t}}^{\substack{\text{Gas phases} \\ \text{accumulation term}}} + \overbrace{\sum_{i=1}^{N_{\mathrm{p}}} \left(\epsilon_i \rho_i c_{\mathrm{p},i} \frac{\partial T}{\partial t} + h_i \underbrace{\frac{\partial \left(\epsilon_i \rho_i\right)}{\partial t}}_{\substack{\text{pyrolysis} \\ \text{products}}} \right)}^{\substack{\text{Solid phases} \\ \text{accumulation term}}} = \overbrace{\frac{\partial}{\partial \boldsymbol{x}} \left(\underline{\underline{\boldsymbol{k}}} \frac{\partial T}{\partial \boldsymbol{x}} \right)}^{\substack{\text{Effective} \\ \text{conduction}}} + \\ &+ \underbrace{\frac{\partial \left(\epsilon_{\mathrm{g}} \rho_{\mathrm{g}} h_{\mathrm{g}} \boldsymbol{v_g}\right)}{\partial \boldsymbol{x}}}_{\substack{\text{Advective} \\ \text{term}}} + \underbrace{\frac{\partial}{\partial \boldsymbol{x}} \left(\sum_{j=1}^{N_{\mathrm{g}}} \mathcal{Q}_j \right)}_{\substack{\text{Heat transport} \\ \text{effective diffusion}}} + \underbrace{\mu \epsilon_{\mathrm{g}}^2 \left(\underline{\underline{\boldsymbol{K}}}^{-1} \cdot \boldsymbol{v_g} \right) \cdot \boldsymbol{v_g}}_{\substack{\text{Heat convection} \\ \text{term}}} + \underbrace{\dot{S}}_{\substack{\text{Source} \\ \text{term}}} \end{aligned} \tag{2.18}$$

where h_g is the specific enthalpy of the gas, p is the pressure, $c_{p,i}$ and h_i are respectively the specific heat capacity and the specific enthalpy of the solid phase i, $\underline{\underline{\boldsymbol{k}}}$ is the conductivity tensor (Fourier's law), $\mathcal{Q}_j$ is the effective diffusion flux of gas species j and $\dot{S}$ is a source term.

2.3.2 Pyrolysis Dimensionless Model

A dimensionless model with a simplified version of the governing equations of pyrolysis has been used for the purpose of this work. This model is also referred as 0D (zero dimensional) model. In a 0D model, temperature is uniform all along the domain. The temperature does not depend on space, but only on time: $T(t)$. The rest of the properties, such as density or specific heat capacity, do not depend on space either. The hypothesis of uniform temperature is valid due to the small size of the crucibles. A demonstration of why the dimensionless model can be used is shown in [31].

The pyrolysis 0D model does not need the mass and momentum equations. Then, the equations are reduced to the kinetic model and to the energy equation. Furthermore, in order to model the contribution of the pyrolysis reaction to the measured c_p, a new definition is added to this model: the apparent heat capacity. The enthalpy of the pyrolysis reaction can also be obtained from this definition.

Kinetic model

The kinetic model used in this 0D model is the one implemented by Lachaud and Mansour [14]. This kinetic model is given by the following expressions:

$$\frac{d\chi_i}{dt} = (1-\chi_i)^{m_i} T^{n_i} A_i \exp\left(-\frac{E_i}{RT_i}\right) \tag{2.19a}$$

$$\rho = \rho_v \left(1 - \sum_{i=1}^{N_p} F_i \chi_i\right) \tag{2.19b}$$

Note that this kinetic model introduces another constant m_i apart from the previously mentioned kinetic triple. F_i is the fraction of density loss in the i^{th} solid phase. In this project, it has been assumed that TACOT undergoes a single pyrolysis reaction, according to Lachaud and Mansour model for this theoretical ablative material [16]: $N_p = 1$.

Energy equation

The energy equation in a 0D case can be obtained by removing all the space-dependent terms in (2.18) and by not considering also the volume fractions, yielding:

$$\overbrace{\frac{\partial\left(\rho_g h_g - p\right)}{\partial t}}^{\substack{\text{Gas phases}\\ \text{accumulation term}}} + \overbrace{\sum_{i=1}^{N_p}\left(\rho_i c_{p,i}\frac{\partial T}{\partial t} + h_i \underbrace{\frac{\partial \rho_i}{\partial t}}_{\substack{\text{pyrolysis}\\ \text{products}}}\right)}^{\substack{\text{Solid phases}\\ \text{accumulation term}}} = \underbrace{\dot{S}}_{\substack{\text{Source}\\ \text{term}}} \tag{2.20}$$

Further simplifications can be made. The conditions inside the experimental facilities allow the experiments to be isobaric, so there is no change of pressure with time. Moreover only one solid phase will be considered, as the objective is to obtain the global c_p. The gas enthalpy, h_g, does not depend on time, so it can be taken out of the time derivative. With all these simplifications, the energy equation is reduced to:

$$\rho c_{\mathrm{p}} \frac{\partial T}{\partial t} + h_{\mathrm{g}} \frac{\partial \rho_{\mathrm{g}}}{\partial t} + h \frac{\partial \rho}{\partial t} = \dot{S} \tag{2.21}$$

Due to mass conservation, the rate of change of the gas density is equal to minus the rate of change of the solid density:

$$\frac{\partial \rho_g}{\partial t} = -\frac{\partial \rho}{\partial t} \tag{2.22}$$

Plugging (2.22) into (2.21):

$$\rho c_{\mathrm{p}} \frac{\partial T}{\partial t} + \left(h - h_{\mathrm{g}}\right) \frac{\partial \rho}{\partial t} = \dot{S} \tag{2.23}$$

The chain rule can be applied:

$$\frac{\partial \rho}{\partial t} = \frac{\partial \rho}{\partial T} \frac{\partial T}{\partial t} \tag{2.24}$$

Then, (2.23) is expressed as follows:

$$\left[\rho c_{\mathrm{p}} + \left(h - h_{\mathrm{g}}\right) \frac{\partial \rho}{\partial T}\right] \frac{\partial T}{\partial t} = \dot{S} \tag{2.25}$$

Apparent heat capacity

The apparent heat capacity is defined from equation (2.25), by dividing the term between brackets by the solid density:

$$c_{\mathrm{p_{Apparent}}} = \underbrace{c_{\mathrm{p}}}_{\substack{\text{Baseline} \\ \text{heat capacity}}} + \underbrace{\frac{h - h_{\mathrm{g}}}{\rho} \frac{\partial \rho}{\partial T}}_{\substack{\text{Pyrolysis} \\ \text{heat capacity}}} \tag{2.26}$$

$c_{\mathrm{p_{Apparent}}}$ is a combination of the baseline c_{p} and the heat released during pyrolysis, which in units of heat capacity is pyrolysis heat capacity. The DSC experiments measure $c_{\mathrm{p_{Apparent}}}$.

Enthalpy of reaction

The enthalpy of reaction, Δh_{pyro}, is obtained by integrating the pyrolysis heat capacity between the temperatures at which the reaction takes place:

$$\Delta h_{\mathrm{pyro}} = \int_{T_0}^{T_{end}} \frac{\left(h - h_{\mathrm{g}}\right)}{\rho} \frac{\partial \rho}{\partial T} \, \mathrm{d}T = \int_{\rho_0}^{\rho_{end}} \frac{\left(h - h_{\mathrm{g}}\right)}{\rho} \, \mathrm{d}\rho \tag{2.27}$$

2.3.3 Thermal Properties Modelling

Calculation of the apparent c_{p} of ablative materials according to equation (2.26) requires knowledge of the baseline c_{p} and h, which are properties of the material. These properties are to be determined so that the apparent c_{p} obtained from simulations fits experimental c_{p} data. They are inputs to the problem: therefore, they need to be modelled by analytical functions, which in turn need to be optimized for determining the apparent c_{p}.

The specific baseline heat capacity is modelled by a function of the following type [22].

$$c_{\mathrm{p}}\left(T\right) = A + B\left(\frac{T}{1000}\right) + C\left(\frac{T}{1000}\right)^2 + D\left(\frac{T}{1000}\right)^3 + \frac{E}{\left(T/1000\right)} \tag{2.28}$$

where A, B, C, D and E are constants to be determined.

$h(T)$ is obtained by using the following relation between $c_{\mathrm{p}}(T)$ and $h(T)$:

$$h(T) = \Delta h^0 + \int_{T_{ref}}^{T} c_{\mathrm{p}}(T)\, \mathrm{d}T \tag{2.29}$$

where Δh^0 is the enthalpy of formation at standard conditions. It is also a constant to be determined. The enthalpy $h(T)$ is then obtained by applying the previous expression to (2.28):

$$\begin{aligned} h(T) = \Delta h^0 + A\left(T - T_{ref}\right) + 500 \cdot B\left[\left(\frac{T}{1000}\right)^2 - \left(\frac{T_{\mathrm{ref}}}{1000}\right)^2\right] + \\ + 333.33 \cdot C\left[\left(\frac{T}{1000}\right)^3 - \left(\frac{T_{\mathrm{ref}}}{1000}\right)^3\right] + 250 \cdot D\left[\left(\frac{T}{1000}\right)^4 - \left(\frac{T_{\mathrm{ref}}}{1000}\right)^4\right] + \\ + 1000 \cdot E \ln\left(\frac{T}{T_{ref}}\right) \end{aligned} \tag{2.30}$$

2.4 Optimization Algorithms

As explained, the constants from expressions (2.28) and (2.30) must be determined as accurately as possible, so that the numerical apparent c_{p} best approximates the experimental apparent c_{p}. This is a difficult problem to tackle, as these constants can take different values depending on the material and the temperature range studied. To solve this problem, optimization algorithms are used. They can explore multiple combinations of the constants and find the ones that best fit expressions (2.28) and (2.30) with experimental data.

Optimization algorithms can be classified in many different ways; a common one is to distinguish between gradient based and gradient free algorithms:

- **Gradient based algorithms**. This family of algorithms compute the gradient of the functions to find the optima. The gradient (or steepest) descent is an example of gradient based algorithm. In this section, the gradient descent is introduced.
- **Gradient free algorithms**. This family of algorithms does not use gradients. Evolutionary algorithms, such as genetic algorithms, and swarm intelligence are included in this type. In this section, the genetic algorithms is introduced.

Optimization aims at minimizing an objective function $F(\boldsymbol{X})$, where $\boldsymbol{X}$ is the vector containing the design variables x_i. The design variables are the set of variables that are changed according to an optimization algorithm, and the optimum solution will be the vector $\boldsymbol{X}$ yielding the minimum value of $F(\boldsymbol{X})$. In general terms, an optimization problem composed by N_{var} design variables can be defined as follows:

Table 2.2: General formulation of an optimization problem [24]

Minimize:			
	Objective function	$F(\boldsymbol{X})$	
where:			
	$\boldsymbol{X} = (x_1, x_2, ..., x_{\mathrm{i}}, ..., x_{\mathrm{N_{var}}})^{\mathrm{T}}$		
subject to:			
	Inequality constraints	$g_j(\boldsymbol{X}) \leq 0,$	$i = 1, 2, ..., m$
	Equality constraints	$h_k(\boldsymbol{X}) = 0,$	$j = 1, 2, ..., p$
	Bounds of variable x_i	$x_i^L \leq x_i \leq x_i^U,$	$i = 1, 2, ..., N_{\mathrm{var}}$

The design variables are restricted within upper and lower bounds, which must be chosen carefully to obtain physically feasible results. The set of all design variables is known as search space. Inequality or equality constraints can be specified in order to restrict the solution. For the purposes of this project, no constraints are defined.

To illustrate the optimization algorithms used in this project, the 2D function shown in Figure 2.3 is used as an example. The function contains level sets whose values decrease up to two optima: a local optimum and a global optimum. The objective is to find the global optimum, as it is the one that minimizes the value of the function $F(\boldsymbol{X})$. The design variable vector $\boldsymbol{X}$ contains the variables x_1 and x_2:

$$\boldsymbol{X} = \left\{ \begin{array}{c} x_1 \\ x_2 \end{array} \right\} \tag{2.31}$$

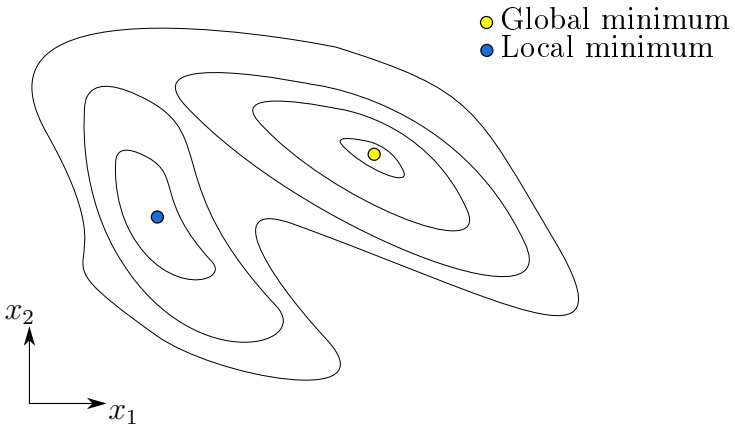

Figure 2.3: 2D function with level sets and two optima.

2.4.1 Genetic Algorithm

Genetic algorithms (GA) are a group of stochastic optimization algorithms which are inspired on the process of Darwin's survival of the fittest, also known as natural selection. Algorithms encompassed inside stochastic optimization use random variables. GA combines stochastic search with storage and manipulation of the design variables. In this way, GA allows both explotation of the best solutions and exploration of the search space [24].

In order to mimic the process of natural selection, a GA codifies the design variables in a binary string called a chromosome. Each design variable is codified as a gene inside the chromosome. A gene contains a number of bits, each one of them is known as an allele. An example of a chromosome C with genes comprised of 8 alleles is shown next:

$$C = \left[\underbrace{10010010}_{\text{Gene 1}} \underbrace{01011110}_{\text{Gene 2}} ... \underbrace{11000010}_{\text{Gene N}} \right] \tag{2.32}$$

The first step in a GA is to define a randomly generated initial population of individuals (or chromosomes). After a generation process in which the GA exchanges incormation between the individuals, a new population is obtained. This process is known as generation. After a generation process, the relatively good solutions are kept, meanwhile the bad solutions disappear.

GA can be summarized in the following steps:

1. **Evaluation**. Each individual is evaluated with a fitness function. This fitness function evaluates the performance of each individual with respect to the other ones.

2. **Selection**. Groups of two individuals (parents) of the population are selected to exchange information and reproduce. Methods such as roulette wheel, linear rank or tournament selection [24, 11] are used to carry out this operation.

3. **Reproduction (cross-over)**. The individuals selected in the previous step exchange information and reproduce, generating new chromosomes. These new chromosomes contain information from their parents, and form a new population of individuals.

4. **Mutation**. As in natural selection, mutation in individuals can occur. If mutation occurs, allels inside a chromosome are inverted. This process is randomly applied with a probability below 1 %.

5. **Elitism**. The new population of individuals is evaluated through the fitness function. The best fit individuals in this population are selected to survive.

6. **Extermination**. The lowest fit individuals are rejected for the next generation and are exterminated. A usual percentage of extermination is between 10 % and 25 % [24].

GA iterates between steps 1 to 6 until a termination criterion is reached. Two termination criteria can be defined in a GA:

- Maximum number of generations. A typical value is 150 [24].
- Convergence of the fitness function. If in a subsequent number of generations (e.g. 10 generations) the fitness function does not change by more than a threshold (e.g. 1×10^{-4} %), the optimization finishes.

Genetic algorithms have the disadvantage that they can take a long time to reach termination. Furthermore, tuning the parameters of the algorithm (reproduction and mutation rates, extermination percentage) is not an easy process, as there are no general rules and it is often done by trial and error.

GA applied to the function of Figure 2.3 is illustrated in Figure 2.4.

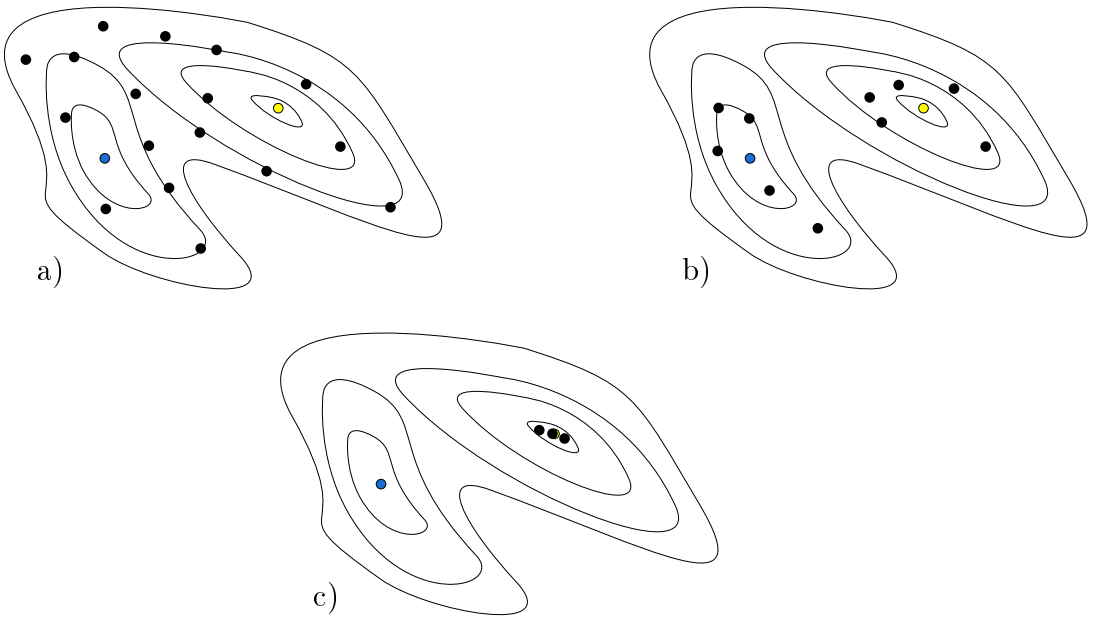

Figure 2.4: Single objective genetic algorithm. a) Initial population. b) Population after some generations. c) Final population after termination.

2.4.2 Gradient Descent Algorithm

Gradient descent, also known as steepest descent, is a family of algorithms in which the search direction of the optimal point is chosen according to the direction in which the objective function $F(\boldsymbol{X})$ decreases more rapidly. This is the direction of the negative of the gradient, $-\nabla F(\boldsymbol{X})$ [20]:

$$\boldsymbol{X}^{\mathrm{k}+1} = \boldsymbol{X}^{\mathrm{k}} - \gamma \nabla F\left(\boldsymbol{X}^{\mathrm{k}}\right) \tag{2.33}$$

where k is the iteration of the algorithm and γ is the step or rate of change. The choice of γ will affect the convergence: a large value of γ might make the algorithm to diverge instead of converging; a small value of γ can yield a long time to converge.

As (2.33) shows, the gradient is evaluated at the current point $\boldsymbol{X}^{\mathrm{k}}$. The next point is calculated towards the negative direction of the gradient at this point. The gradient descent algorithm is illustrated in Figure 2.5.

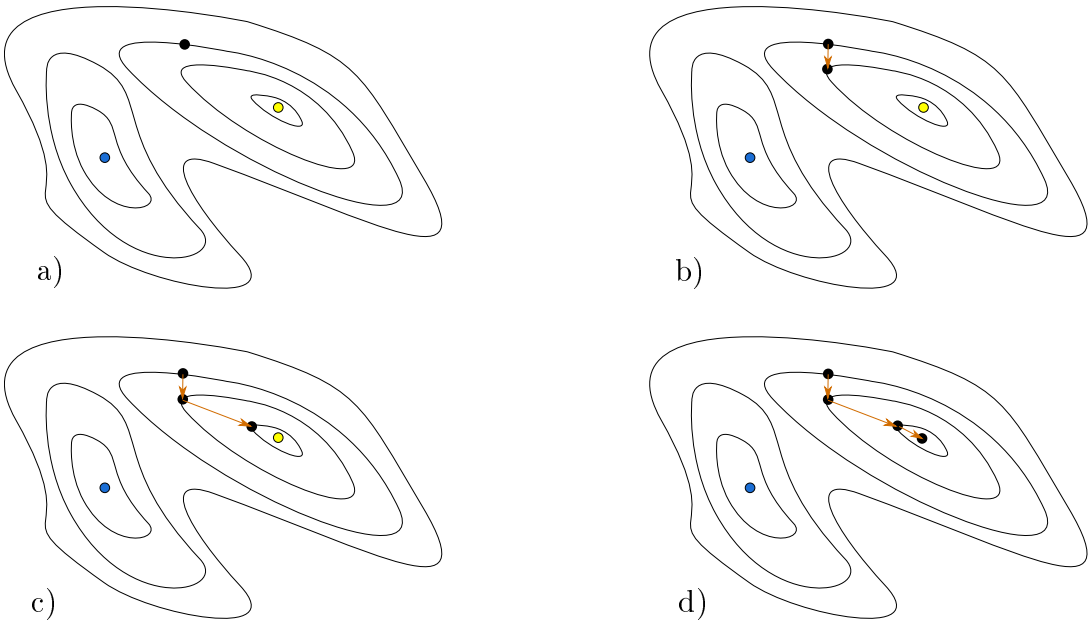

Figure 2.5: Gradient descent algorithm. The choice of initial point in a) converges to the global optimum in d)

Shortcoming of the Gradient Descent

The gradient descent algorithm presents one main disadvantage. If the initial point is not properly chosen, the algorithm can converge to the local optimum and get stuck there (Figure 2.6).

The choice of initial point can be difficult, specially if there is not much information available about the problem. Nevertheless, this problem (and hence the shortcoming of the gradient descent) can be avoided by choosing what is known as a hybrid approach.

2.4.3 Hybrid Approach

A hybrid approach combines different algorithms with the objective of converging faster to the global optimum. GA and the gradient descent can be combined in a hybrid approach as follows:

1. Firstly, GA is applied as explained previously. The result of this step is a point in the region of the global optimum as shown in Figure 2.4c.

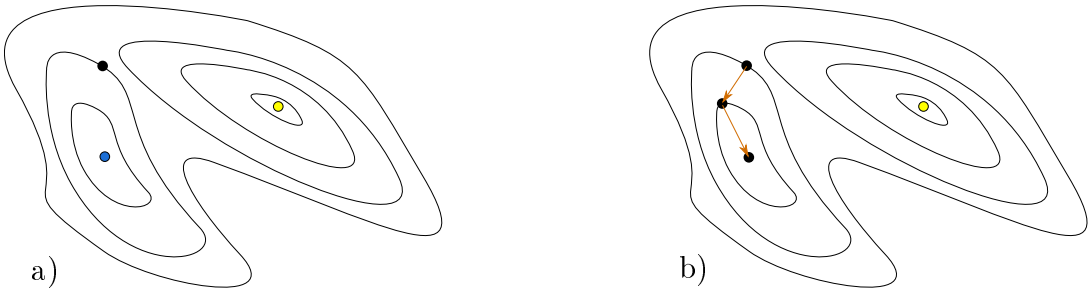

Figure 2.6: Gradient descent algorithm. The choice of initial point in a) converges to the local optimum in b). The algorithm stops when reaching the local optimum: the global optimum is never obtained.

2. Secondly, the solution obtained by the GA is used as the initial point for the gradient descent. The gradient descent converges then rapidly to the global optimum.

This approach, used in this project, combines the advantages of both algorithms and avoids the shortcoming of the gradient descent: all the search space is explored and the most optimal region is found with the GA, and then the gradient descent converges fastly without getting stuck into a local optimum.

2.4.4 Fitness Function

The fitness function J is used to compare experimental and numerical data: it is a measure of the optimization convergence. It is given by the following expression:

$$J = \sum_{\mathrm{i}=0}^{\mathrm{N}} \sqrt{\left(\frac{c_{\mathrm{pPATO_i}} - c_{\mathrm{pDSC_i}}}{\max\left\{ c_{\mathrm{pDSC_i}} \right\}} \right)^2} \tag{2.34}$$

where N is the number of experimental data points, $c_{\mathrm{pDSC_i}}$ is the experimental apparent heat capacity, and $c_{\mathrm{pPATO_i}}$ is the numerical apparent heat capacity. The best fit between experimental apparent c_{p} data and numerical apparent c_{p} minimizes the value of the fitness function.

2.5 Bayesian Inference and Uncertainty Quantification

Uncertainty Quantification (UQ) is used to ensure that the outcome of the simulations is within a certain range. The true c_{p} will not be certainly characterized by a single function, but within a region in which the true value is found. To perform UQ, Bayesian inference is used.

Bayesian inference is a branch of statistics in which previous observations, or evidences, of a system are used to infer probability statements about the future state of that system. In Bayesian inference true is not considered to be given by a single statement, but by a set of possible statements. Probabilities are used to characterize the state of the system.

Let's consider a system characterized by a set of parameters $\boldsymbol{\theta}$. This system produces an output $\boldsymbol{y}$, also known as the observed data of the system. There is no true parameter in the Bayesian approach; hence, both $\boldsymbol{\theta}$ and $\boldsymbol{y}$ are considered vectors of random variables that follow probability distributions.

Bayesian inference is based on Bayes theorem:

$$p\left(\boldsymbol{\theta}|\boldsymbol{y}\right) = \frac{p\left(\boldsymbol{y}|\boldsymbol{\theta}\right) p\left(\boldsymbol{\theta}\right)}{p\left(\boldsymbol{y}\right)} = \frac{p\left(\boldsymbol{y}|\boldsymbol{\theta}\right) p\left(\boldsymbol{\theta}\right)}{\int p\left(\boldsymbol{y}|\boldsymbol{\theta}\right) p\left(\boldsymbol{\theta}\right) \, \mathrm{d}\boldsymbol{\theta}} \tag{2.35}$$

where $p(\boldsymbol{\theta})$ is the prior probability density function (PDF), $p(\boldsymbol{y}|\boldsymbol{\theta})$ is the likelihood function and $p(\boldsymbol{\theta}|\boldsymbol{y})$ is the posterior PDF. The integral in the denominator normalizes the numerator so that the integral of the posterior PDF over its range is 1 [5].

The prior PDF $p(\boldsymbol{\theta})$ represents what is known about the parameters θ **before** any computation is made. The likelihood function $p(\boldsymbol{\theta})$ is a proposed function that evaluates the possibility of observing the data $\boldsymbol{y}$ given the parameters $\boldsymbol{\theta}$ through the model of the system which connects $\boldsymbol{y}$ and $\boldsymbol{\theta}$. The posterior PDF $p(\boldsymbol{\theta}|\boldsymbol{y})$ represents what is known about the parameters **after** computations are made. The objective of Bayesian inference is to pinpoint this posterior PDF, as it contains all the information on how the parameters θ affect the output of the system. UQ can be performed with this information.

The most widely used algorithms for Bayesian inference are Markov Chain Monte Carlo (MCMC).

2.5.1 Markov Chains

A Markov Chain can be defined as a time-variant process in which the state of the process at a given time t depends only on its immediately previous state $t-1$. The values of the process at time instants previous to $t-1$ do not influence its behaviour in the subsequent time steps [23].

Figure 2.7 shows a Markov Chain representing a 3 states process: A, B and C. The arrows show the interaction between the processes. Each arrow has a number representing the probability of that transition taking place. For example, state A has a 70 % of probability of moving to state B, and a 30 % of probability of moving to state C. States B and C also present probabilities of staying at the same state.

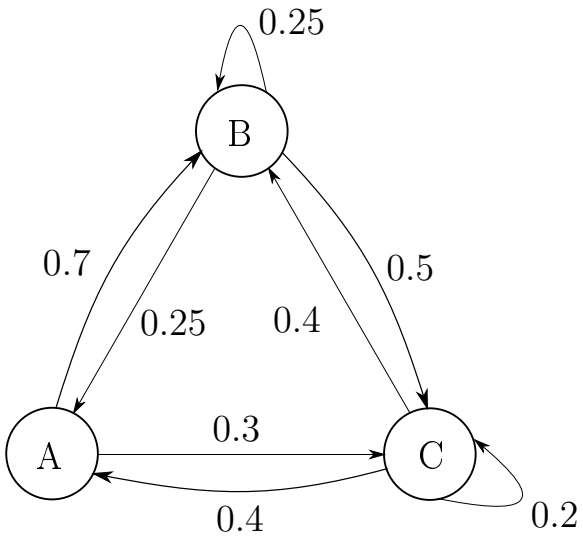

Figure 2.7: Markov Chain of 3 states.

2.5.2 Monte Carlo Sampling

Monte Carlo sampling, is a technique used to draw samples from a given distribution or function. To extract these samples, the Monte Carlo algorithm just generates randomly distributed numbers and evaluates the function at those points. Due to this, sometimes it is also referred as the *brute force* approach. Monte Carlos algorithm cannot be considered an optimization algorithm by itself, but a sampling method.

2.5.3 Markov Chain Monte Carlo Algorithm

Markov Chain Monte Carlo (MCMC) algorithm combines both Monte Carlo sampling with Markov Chains. The algorithm draws random samples of a parameter θ from a probability distribution in which every sample depends only on the previously obtained sample, but not on the former ones; this is the Markov Chain part. The samples are randomly drawn from the probability distribution function; this is the Monte Carlo part.

The MCMC algorithm is useful for generating samples of the parameters of interest from an arbitrary distribution [28]. These parameters will be the design variables of the objective function to minimize. The samples are then used to evaluate how sensitive the objective function is to changes in the inputs. The problem will then be characterized in terms of probability distributions for the input parameters, and uncertainties in the outputs will be quantified in statistical terms.

A well-known MCMC algorithm is the Metropolis-Hastings (MH) algorithm, shown in the following table:

Table 2.3: Metropolis-Hastings algorithm [6]

Step 1 **Initialize** $\boldsymbol{\theta}_0$

Step 2 **Iteration** k:

a) Draw a new value $\boldsymbol{\theta}^*$ from a proposal distribution q

b) Calculate acceptance ratio r

$$r = \frac{p\left(\boldsymbol{\theta}^*|\boldsymbol{y}\right) q\left(\boldsymbol{\theta}_{\mathrm{k}-1}|\boldsymbol{\theta}^*\right)}{p\left(\boldsymbol{\theta}_{\mathrm{k}-1}|\boldsymbol{y}\right) q\left(\boldsymbol{\theta}^*|\boldsymbol{\theta}_{\mathrm{k}-1}\right)} = \frac{p\left(\boldsymbol{y}|\boldsymbol{\theta}^*\right) p\left(\boldsymbol{\theta}^*\right) q\left(\boldsymbol{\theta}_{\mathrm{k}-1}|\boldsymbol{\theta}^*\right)}{p\left(\boldsymbol{y}|\boldsymbol{\theta}_{\mathrm{k}-1}\right) p\left(\boldsymbol{\theta}_{\mathrm{k}-1}\right) q\left(\boldsymbol{\theta}^*|\boldsymbol{\theta}_{\mathrm{k}-1}\right)}$$

where Bayes theorem, expression (2.35), has been introduced.

c) Get acceptance probability $\alpha\left(\boldsymbol{\theta}^*|\boldsymbol{\theta}_{\mathrm{k}-1}\right)$

$$\alpha\left(\boldsymbol{\theta}^*|\boldsymbol{\theta}_{\mathrm{k}-1}\right) = \min\left(1, r\right)$$

c) Sample a uniform random variable between 0 and 1: $u \sim U_{[0,1]}$

e) Set new parameters according to the following criterion

$$\boldsymbol{\theta}_{\mathrm{k}} = \begin{cases} \boldsymbol{\theta}^* & u \leq \alpha\left(\boldsymbol{\theta}^*|\boldsymbol{\theta}_{\mathrm{k}-1}\right) \\ \boldsymbol{\theta}_{\mathrm{k}-1} & \text{otherwise} \end{cases}$$

Step 3 **Continue until enough samples are collected**

A particular case of the MH algorithm is the random walk. In the random walk the proposal distribution is considered to be symmetric: $q\left(\boldsymbol{\theta}_{\mathrm{k}}|\boldsymbol{\theta}^*\right) = q\left(\boldsymbol{\theta}^*|\boldsymbol{\theta}_{\mathrm{k}}\right)$. Also, a uniform prior PDF is assumed: $p\left(\boldsymbol{\theta}^*\right) = p\left(\boldsymbol{\theta}_{\mathrm{k}-1}\right)$. In that case the acceptance ratio r is reduced to the following expression:

$$r = \frac{p\left(\boldsymbol{y}|\boldsymbol{\theta}^*\right)}{p\left(\boldsymbol{y}|\boldsymbol{\theta}_{\mathrm{k}-1}\right)} \tag{2.36}$$

Chapter 3

Numerical tool for c_{p} determination of ablative materials

3.1 Description

In this project, a numerical tool to separate the contributions from both thermodynamics and chemistry in DSC experimental data has been developed. This will allow for the determination of the heat capacity of ablative materials.

Experiments and numerical simulations have been combined through the flowchart of Figure 3.1. It is composed of three main parts: the pyrolysis solver (represented by the block *Solver*); the apparent heat capacity versus temperature obtained with DSC experiments (represented by the block *Experiments*); and the optimization loop (represented by the rest of the blocks).

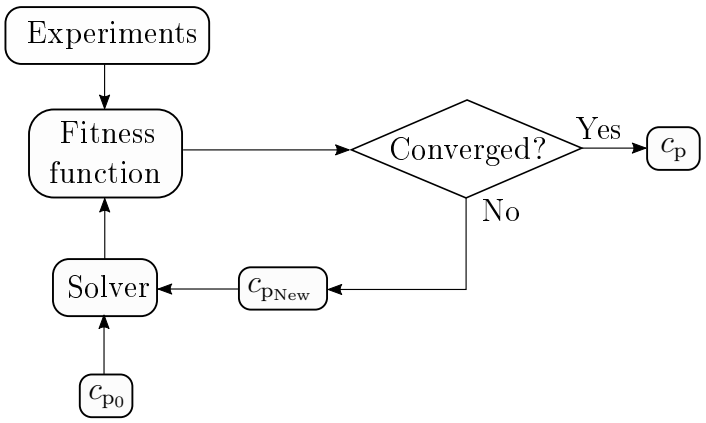

Figure 3.1: Flowchart combining numerics and experiments.

The numerical loop is initialised with an initial value of the c_{p}: c_{p0}. The subscript 0 denotes initial conditions. This value is actually represented by initial value of the constants defined in the model; for example, if the model chosen for the specific heat capacity is given by expression (2.28), initial values for the constants A to E must be given, and c_{p0} is given as follows:

$$c_{\mathrm{p0}}(T) = A_0 + B_0\left(\frac{T}{1000}\right) + C_0\left(\frac{T}{1000}\right)^2 + D_0\left(\frac{T}{1000}\right)^3 + \frac{E_0}{(T/1000)} \tag{3.1}$$

This initial heat capacity is the input of the pyrolysis solver, which then solves the equations of the pyrolysis 0D model. The output is the apparent heat capacity, which is then plugged into the fitness function J given by (2.34). The value of the fitness function is compared to

the termination criteria defined in the optimizer: if termination (i.e. convergence) is reached, then the process stops and the specific heat capacity $c_p(T)$ given by equation (2.28) is obtained; otherwise, new values for the constants A to E are given by the optimization algorithm, and the process is repeated until convergence.

The following sections describe in more detail the pyrolysis solver, the optimizer and their implementation.

3.2 Pyrolysis Solver: PATO

The OpenFOAM library, *Porous Material Analysis Toolbox* (PATO), has been used as pyrolysis solver. PATO is an open-source solver for the pyrolysis and ablation modelling of porous materials. It was created by Lachaud and Mansour [14] at NASA Ames Research Center, and it is one of the most advanced pyrolysis and ablation solvers. Current applications of PATO include the study of LCA used as TPS [31] and the pyrolysis of wood for biomass applications [21].

The pyrolysis solver corresponds to the *Solver* block of the flowchart shown in Figure 3.2.

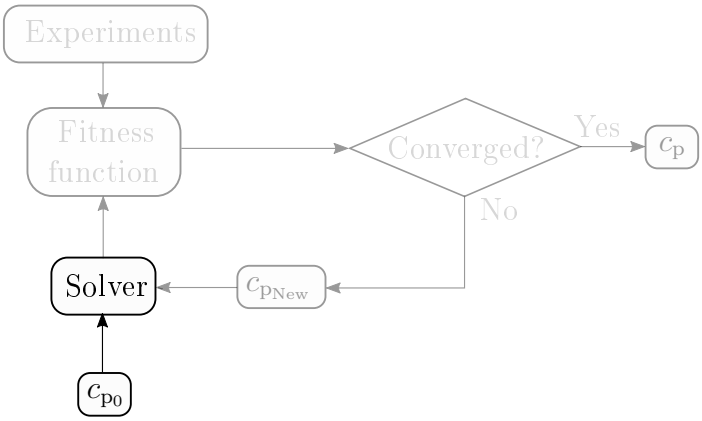

Figure 3.2: Pyrolysis solver (PATO) location in the flowchart.

PATO needs the properties of the material as an input to solve the equations of the pyrolysis model, thus the need of specifying an initial specific heat capacity c_{p0}. Properties of both the virgin and char phases must be specified, as well as the gas properties and the properties of the pyrolysis reactions. Hence, four files need to be specified in PATO with the following information:

- **Char material**. This file contains a table where the properties of the char phase of the material are specified as a function of temperature, such as: specific heat capacity, enthalpy and conductivity.
- **Virgin material**. This file contains a table where the properties of the virgin phase of the material are specified as a function of temperature. The properties specified are the same as in the char material file.
- **Constant properties**. This file contains constants (such as the gas constant R) and the parameters of the reactions m, n, A and E, as well as the number of reactions.
- **Gas properties**. This file contains a table where the properties of the gas released due to pyrolysis are specified as a function of temperature, such as: specific heat, enthalpy, molar mass and viscosity.

When pyrolysis starts to take place, both char and virgin phases coexist. In that case the properties are calculated as a weighted average of the corresponding properties of both individual

phases. For example, the specific heat capacity c_p is calculated from the specific heat capacity of the char, $c_{\mathrm{p_c}}$, and virgin, $c_{\mathrm{p_v}}$, phases as follows:

$$c_\mathrm{p}(T) = \frac{\rho}{\rho_\mathrm{v}} c_{\mathrm{p_v}}(T) + \left(1 - \frac{\rho}{\rho_\mathrm{v}}\right) c_{\mathrm{p_c}}(T) \tag{3.2}$$

The same applies to the enthalpy:

$$h(T) = \frac{\rho}{\rho_\mathrm{v}} h_\mathrm{v}(T) + \left(1 - \frac{\rho}{\rho_\mathrm{v}}\right) h_\mathrm{c}(T) \tag{3.3}$$

It follows from Eq. (3.2) that the heat capacity defined in Eq. (2.28) needs to be specified not for the whole material, but for the char and virgin phases. The same applies to the enthalpy defined in Eq. (2.30). Initially, it can be considered that the char and virgin phases have the same properties ($c_{\mathrm{p_v}} = c_{\mathrm{p_c}}$, $h_\mathrm{v} = h_\mathrm{c}$), so a general expression for the whole material is obtained. In this case the value of the enthalpy of formation Δh^0 would not make physical sense. A more accurate approach is to consider that the properties of the char and virgin phases are different ($c_{\mathrm{p_v}}$, $c_{\mathrm{p_c}}$, h_v and h_c), adding more design variables to the optimization problem.

Solvers have been created in PATO to include the dimensionless 0D model for pyrolysis used here. In this model, $c_{\mathrm{p_{Apparent}}}$ has been defined and specified as an output.

3.3 Optimization Toolbox: Dakota

For the optimization process, the toolbox Dakota has been used. Dakota has been developed by Sandia National Laboratories [1]. It is a software which allows for optimization, calibration, sensitivity analyses and uncertainty quantification. The optimization process performed by Dakota corresponds to the highlighted parts of the flowchart shown in Figure 3.3.

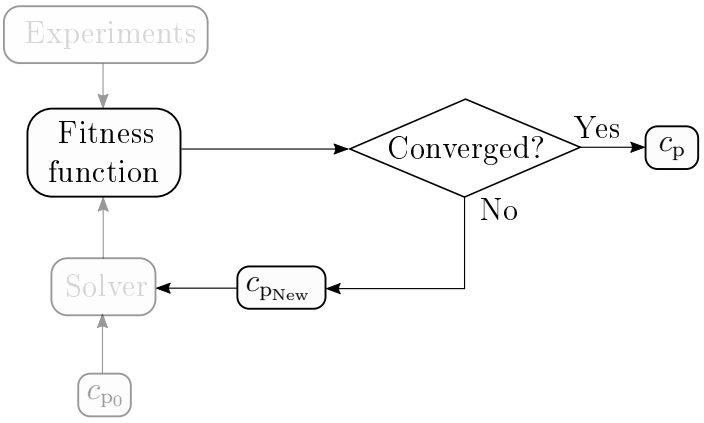

Figure 3.3: Optimization process location in the flowchart.

Dakota input is the optimization problem stated in Table 2.2. In this work, the objective function is the fitness function defined in (2.34), and the variables are the ones defined in expressions (2.28) and (2.30). Considering this and taking into account that there are no constraints, the optimization problem in Dakota can be stated as shown in Table 3.1.

The optimization algorithm must be defined in Dakota: in this work, both the gradient descent and the hybrid approach are used. The algorithm works by providing and changing the values of the design variables from the vector $\boldsymbol{X}$. From these values, the heat capacity that is used in the PATO material files (virgin and char phases) is obtained. The link between Dakota and PATO is performed via a Perl script that introduces the values provided by Dakota into templates of the material files. These templates include the expressions (2.28) and (2.30). The script then performs the operations to calculate $c_\mathrm{p}(T)$ and $h(T)$, creates new templates and

Table 3.1: Formulation of optimization problem for Dakota

Minimize:		
	Objective function	$J(\boldsymbol{X})$
where:		
	$\boldsymbol{X} = \left(A, B, C, D, E, \Delta h^0\right)^{\mathrm{T}}$	
subject to:		
	Bounds of variable x_i	$x_i^L \leq x_i \leq x_i^U, \quad i = 1, 2, ..., N_{\mathrm{var}}$

sets a pyrolysis case. The Case is then run in PATO, which provides Dakota the apparent heat capacity $c_{\mathrm{p_{PATO}}}(T)$ as an output. Dakota then continues with the rest of the loop: calculates the fitness function by comparing with the experimental data $c_{\mathrm{p_{DSC}}}(T)$ and checks the termination criterion. If convergence has not been reached, the algorithm calculates new values for the design vector $\boldsymbol{X}$ and continues with the iteration; if convergence has been reached, the optimization process ends and provides with the optimal solution of the baseline heat capacity, $c_{\mathrm{p}}(T)$.

3.4 Code Verification

Graphite and TACOT materials have been used for verification of the numerical tool developed in this work.

In the case of **graphite**, only one optimization has been performed to model c_{p}. As graphite does not undergo pyrolysis, only one phase of the material has been considered. Furthermore, Uncertainty Quantification by means of Bayesian Inference has been performed to study how the c_{p} model defined in (2.28) responds to changes in the inputs.

On the other hand, different cases have been established for **TACOT** optimization. Initially, only $c_{\mathrm{p}}(T)$ was modelled with expression (2.28) in order to study a reference case with few design variables. In this first case, tabulated values for $h(T)$ and the pyrolysis model of TACOT were used [16].

Next, complexity of the optimization problem was increased by including the modellization of $h(T)$ according to equation (2.30). This second case is compared with the first case in order to get an idea of the inaccuracies arising when introducing $h(T)$. In case this numerical tool is applied to real (not dummy) experimental DSC data, $h(T)$ will not be known; therefore, knowing the effect of considering $h(T)$ is important to get an idea of the code accuracy under these real conditions.

Finally, the kinetic model of pyrolysis, given by equations (2.19a) and (2.19b), was included in the optimization problem. Pyrolysis reactions are not actually known, so introducing them into the model checks how accurately the code can predict them. Initially the parameter F of equation (2.19b) is introduced to model only the density loss. Then, parameters A and E of equation (2.19a) are considered to model also the advancement of reaction. A last case is settled where the enthalpy is modelled together with the density loss.

Additionally, two different sets of cases have been considered, regarding the properties of the char and virgin phases of TACOT: the first set of cases considers them to be equal, thus $c_{\mathrm{p_c}} = c_{\mathrm{p_v}}$ and $h_{\mathrm{c}} = h_{\mathrm{v}}$. In the second set of cases, properties of the char and virgin phases are considered to be different: $c_{\mathrm{p_c}} \neq c_{\mathrm{p_v}}$, $h_{\mathrm{c}} \neq h_{\mathrm{v}}$. The averaged $c_{\mathrm{p}}(T)$ given by (3.2) and averaged $h(T)$ given by (3.3) are then obtained.

In summary, the different cases that have been studied for TACOT can be classified as follows:

- Modelling of solid enthalpy: $h(T)$ modelled or not.
- Pyrolysis reactions modelled or not.

- Different values of the properties of char and virgin phases, or simplification by considering them to be equal.

The different cases that have been defined and optimized for TACOT are shown in Table 3.2.

Table 3.2: TACOT test cases

Objective	Case	Enthalpy modelled?	Pyrolysis reactions modelled?	Char and virgin phases identical?
Effect of modelling enthalpy	1	No	No	Yes
	2	Yes	No	Yes
Effect of modelling pyrolysis	3	No	Yes	Yes
	4	No	Yes	Yes
	5	Yes	Yes	Yes
Effect of differentiating properties of char and virgin phases	6	No	No	No
	7	No	No	No
	8	Yes	No	No

3.4.1 Graphite Test Case

Experimental c_p

The heat capacity of graphite is given by the following expression [22]:

$$c_p(T) = -333.33 + 4095.83\left(\frac{T}{1000}\right) - 2553.33\left(\frac{T}{1000}\right)^2 + 570.83\left(\frac{T}{1000}\right)^3 \tag{3.4}$$

This expression is plotted in Figure 3.4 between 298 and 1400 K.

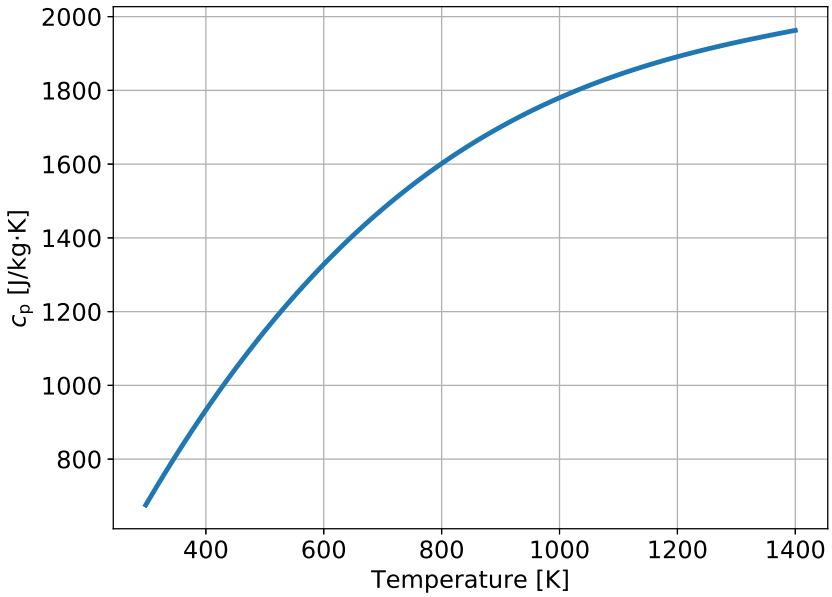

Figure 3.4: Graphite heat capacity

Comparing expressions (3.4) and (2.28), the constants for graphite take the following values:

Table 3.3: Graphite tabulated constants [22]

Constant	Value
A	-333.33
B	4095.83
C	-2553.33
D	570.83
E	0

Due to the fact that no pyrolysis reactions take place in graphite, the pyrolysis heat capacity term in equation (2.26) is 0. Consequently, the apparent and the baseline heat capacity are identical.

$$c_{\mathrm{pApparent}} = c_{\mathrm{pBaseline}} \tag{3.5}$$

Note also that because the pyrolysis heat capacity is 0, the enthalpy of the graphite plays no role and it does not need to be modelled. Therefore, only expression (2.28) for c_p of graphite is optimized.

In order to simulate dummy data, gaussian noise is added to the heat capacity of graphite. Gaussian noise follows a probability distribution centered at $\mu = 0$ with a standard deviation σ given by the following probability density function:

$$p(x) = \frac{1}{\sigma\sqrt{2\pi}} \exp\left(-\frac{x^2}{2\sigma^2}\right) \tag{3.6}$$

Gaussian noise is generated between 298 and 1400 K and added to the curve of Figure 3.5, yielding the green line. The noise standard deviation is $\sigma = 25$. The noisy heat capacity represents the data coming from experiments.

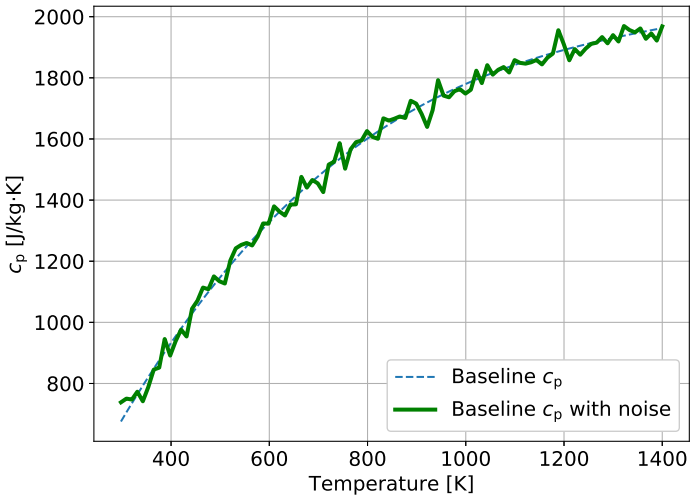

Figure 3.5: Dummy data for graphite heat capacity

Optimized c_p

The objective of the optimization is to approximate constants A to D used in equation (2.28) to the values shown in Table 3.3. The gradient descent algorithm has been used with a termination

criterion based on a convergence tolerance of 10^{-6}. Results of the optimization are shown in Table 3.4 and Figure 3.6.

Table 3.4: Graphite constants

Constant	Tabulated value	Optimal value	Difference [%]
A	-333.33	-302.88	9.10
B	4095.83	4186.58	2.22
C	-2553.33	-2785.52	-9.09
D	570.83	683.16	19.68

It can be seen that the largest difference is in constant D: almost 20 % of difference with respect to its tabulated value. This difference is considerable: the expression obtained by plugging the optimal constants into equation (2.28) should not be extrapolated to temperatures outside the range studied. The optimized c_p line shows that there is a bias at low temperatures with respect to the baseline c_p; however, the noisy c_p at low temperatures is closer to the optimized line than to the baseline, which means that the optimized c_p tends to fit it. At high temperatures the optimized c_p is almost spotless: it matches the baseline c_p. It can then be concluded that the code works adequately for graphite.

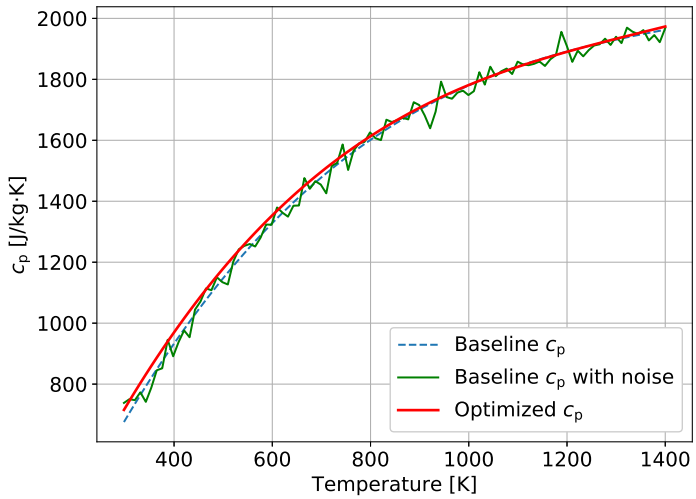

Figure 3.6: Graphite specific heat capacity optimization

Uncertainty Quantification

UQ has been done by means of the Metropolis-Hastings random-walk algorithm. The vector of parameters θ contains coefficients A, B, C and D. The vector will be initialized with the constants obtained from the optimization of graphite shown in Table 3.4:

$$\theta_0^T = (-302.88 \quad 4186.58 \quad -2785.52 \quad 683.16) \tag{3.7}$$

A uniform prior distribution is assumed for the parameters. Therefore, according to (2.36), the prior distribution does not need to be computed because its ratio is 1.

The proposal distribution from which the parameters $\boldsymbol{\theta}_k$ are sampled is a multivariate gaussian distribution centered at $\boldsymbol{\theta_{k-1}}$:

$$q\left(\boldsymbol{\theta}^*|\boldsymbol{\theta}_{k-1}\right) = \frac{1}{\sigma\sqrt{2\pi}} \exp\left(-\frac{\left(\boldsymbol{\theta}^* - \boldsymbol{\theta}_{k-1}\right)^T \left(\boldsymbol{\theta}^* - \boldsymbol{\theta}_{k-1}\right)}{2\sigma^2}\right) \tag{3.8}$$

where the standard deviation σ is the standard deviation of the gaussian noise.

The likelihood function defines a distribution for the observation errors: the difference between the observations $\boldsymbol{y}$ and the output of the simulations. These observations are the data coming from the experiments. Therefore, $\boldsymbol{y}$ represents the dummy data heat capacity: $\boldsymbol{y} = \boldsymbol{c_{pDSC}}$. The observation errors are assumed to follow a normal distribution, so the likelihood function is given by:

$$p\left(\boldsymbol{y}|\boldsymbol{\theta}\right) = \frac{1}{\sigma\sqrt[N]{2\pi}} \exp\left(-\sum_{i=1}^{N} \frac{\left(c_{pPATO_i} - c_{pDSC_i}\right)^2}{2\sigma^2}\right) \tag{3.9}$$

The Metropolis-Hastings random walk has been run for 10^6 iterations. Results for the samples propagation are shown in Figure 3.7. The green shaded area contains all the possible values for c_p given by all the possible combinations of the parameters A to D. The medium fit line is the average of all the c_p combinations obtained. The confidence interval is the region in which the real value for the c_p might be contained. The upper and lower values are calculated by adding and substracting two times the noise standard deviation to the medium fit line: $c_p^{Medium} \pm 2\sigma$. All the possible values for the c_p are contained within the confidence interval: this guarantees that the real c_p is certainly located within the green shaded area.

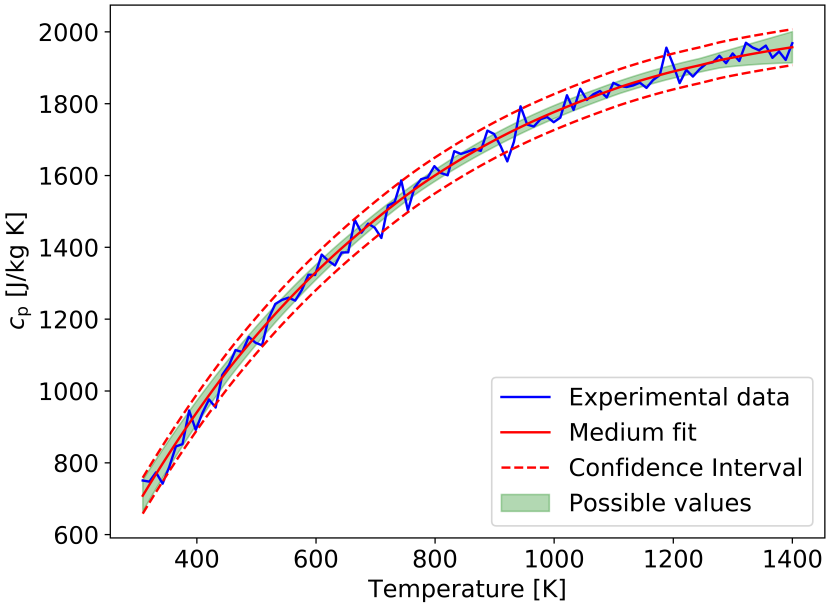

Figure 3.7: Specific heat capacity propagation results: medium fit, confidende interval and region containing possible baseline c_p values. Experimental data for graphite are also shown.

3.4.2 TACOT Test Case

Experimental c_p

TACOT properties are tabulated with temperature [16]. $c_p(T)$ of TACOT is given by the heat capacities of the char (c_{p_c}) and virgin (c_{p_v}) phases (Figure 3.8).

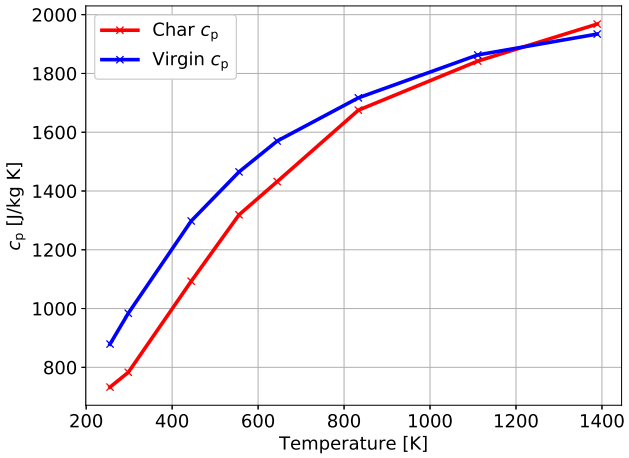

Figure 3.8: Specific heat capacity of char and virgin phases of TACOT

Equation (3.2) is then applied to c_{p_c} and c_{p_v} in order to obtain the averaged specific heat of TACOT (blue line of Figure 3.9). The constants from the kinetic model presented in equations (2.19a) and (2.19b) have been defined by Lachaud [16]: $A = 12000$, $E = 71\,130\,\mathrm{J/mol}$, $F = 0.25$. These constants are needed in order to obtain how the advancement of reaction and density change with temperature. Then, the apparent heat capacity is obtained by adding the pyrolysis heat capacity as defined in (2.26), yielding the black line of Figure 3.9.

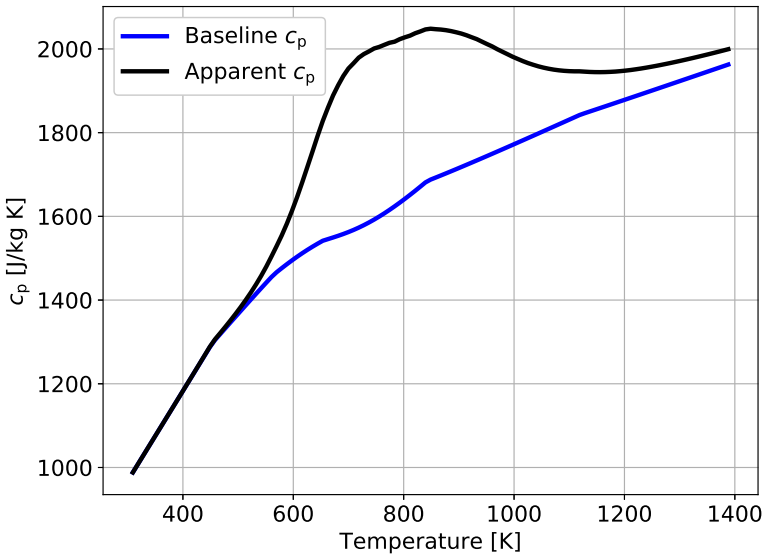

Figure 3.9: Averaged specific heat capacity of TACOT

Effect of modelling enthalpy

Initially, char and virgin phases are assumed to be equal, and the pyrolysis reactions are not modelled. The optimization algorithm used is the gradient descent. Two cases are then defined, depending on whether the enthalpy is modelled or not:

- **Case 1**. The enthalpy is not modelled. Therefore, only $c_p(T)$ is modelled and the total number of variables to optimize is 5: constants A to E from equation (2.28)
- **Case 2**. The enthalpy is modelled according to equation (2.30). The total number of variables to optimize is 6: constants A to E from $c_p(T)$ model and constant Δh^0 from $h(T)$ model.

The resulting values of the constants and fitness function obtained after optimization are displayed in Table 3.5. Optimized c_p curves for both cases are shown in Figure 3.10.

Table 3.5: Effect of modelling enthalpy: constants and fitness function.

Constant	Case 1	Case 2
A	52.08	6.17
B	3707.13	3779.43
C	-2745.26	-2766.39
D	761.99	750.36
E	19.53	28.31
Δh^0 [J/kg]	-	-7.364×10^6
J	4.25	6.60

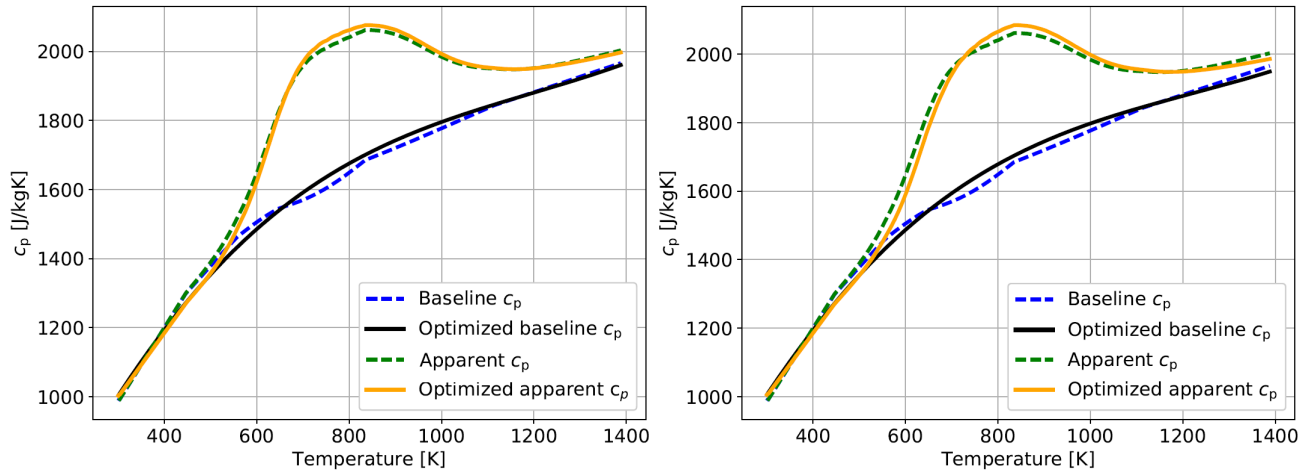

a) b)

Figure 3.10: Effect of modelling enthalpy: baseline c_p and apparent c_p. a) Case 1. b) Case 2.

The fitness function increases when modelling the enthalpy. Therefore, introducing the variable Δh^0 reduces the optimization accuracy. Although approximation to the baseline c_p is relatively good in both cases, the apparent c_p given by PATO fits better the dummy data when the model does not take into account the enthalpy (case 1). Furthermore, not modelling the enthalpy improves the optimization of the heat capacities at high and low temperatures.

Effect of modelling pyrolysis reactions

Next, char and virgin phases are still assumed to be equal, but now the pyrolysis reactions are modelled. Hybrid approach algorithm has been used for optimization. Three cases are then defined, depending on whether the enthalpy is modelled or not and the equations used for modelling pyrolysis:

- **Case 3**. The enthalpy is not modelled. The density loss during pyrolysis is modelled according to equation (2.19b). The total number of variables to optimize is 6: constants A to E from $c_p(T)$ model and constant F_{pyro} from the kinetic model. The subscript pyro is used to properly identify pyrolysis constants.
- **Case 4**. The enthalpy is not modelled. Both the advancement of reaction and the density loss during pyrolysis are modelled according to equations (2.19a) and (2.19b), respectively. The total number of variables to optimize is 8: constants A to E from $c_p(T)$ model and constants A_{pyro}, E_{pyro} and F_{pyro} from the kinetic model.
- **Case 5**. The enthalpy is modelled. The density loss during pyrolysis is modelled according to equation (2.19b). The total number of variables to optimize is 7: constants A to E from $c_p(T)$ model,constant F_{pyro} from the kinetic model and constant Δh^0 from $h(T)$ model.

Optimization results of these cases are shown in Table 3.6 and Figure 3.11.

Table 3.6: Effect of modelling pyrolysis: constants and fitness function

Constant	Case 3	Case 4	Case 5
A	91.54	455.53	13.03
B	3623.83	2429.63	3876.14
C	-2707.84	-1235.30	-2517.45
D	766.25	158.46	518.99
E	18.25	1.37×10^{-2}	10.99
F_{pyro}	0.253	0.252	0.149
A_{pyro}	-	10 150.59	-
E_{pyro} [J/mol]	-	6.9339×10^4	-
Δh^0 [J/kg]	-	-	-7.712×10^6
J	3.89	6.77	4.13

In order to analyse the effect of modelling pyrolysis reactions, cases 3 and 4 are compared with case 1. Comparison of cases 1 and 3 shows that optimization of the density loss during pyrolysis (by including F_{pyro} constant) reduces the fitness function (Tables 3.5 and 3.6), and improves approximation to baseline c_p and apparent c_p (Figures 3.10a and 3.11a). In contrast, comparison of cases 1 and 4 shows that when both the fraction of density loss and the advancement of reaction are optimized, the accuracy decreases significantly, as shown by the increase of the fitness function (Tables 3.5 and 3.6). In case 4, although accurate fit of the apparent c_p is observed from the onset of the pyrolysis reaction (around 500 K) up to 1100 K, apparent c_p and baseline c_p deviate considerably at low and high temperatures (Figure 3.11b). In particular, it is noted that the optimized baseline c_p decreases at high temperatures. This makes no physical sense, as the baseline c_p should always increase with temperature. It can therefore be concluded that adding more variables to the kinetic model improves prediction of the onset of the pyrolysis reaction, but leads to a baseline c_p with no physical sense. This can be attributed to the 0D model used, which implements a simplified version of the governing equations of pyrolysis. Accuracy of the optimizations will be most probably improved by increasing the complexity of the pyrolysis model.

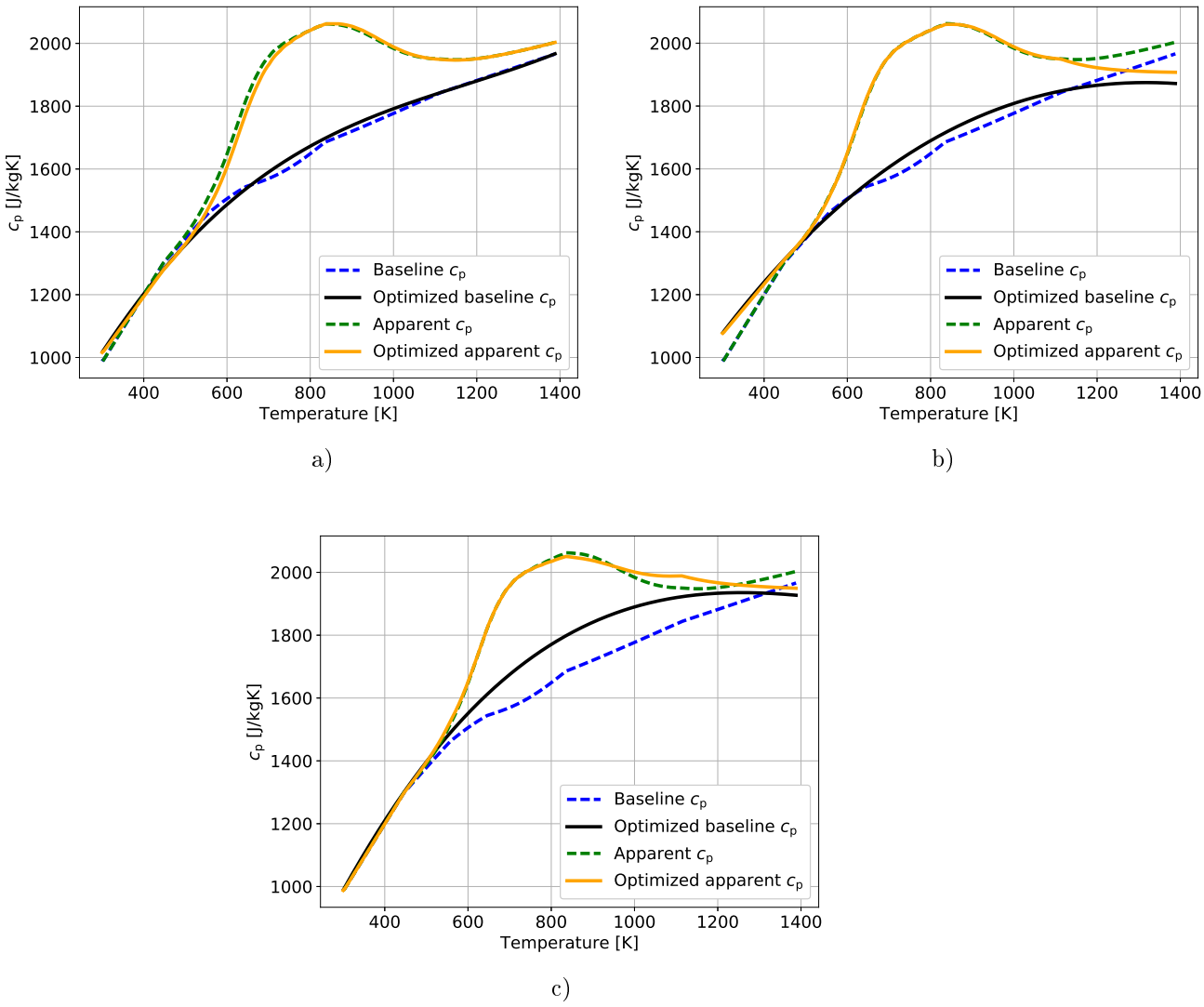

Figure 3.11: Effect of modelling pyrolysis reactions: baseline c_p and apparent c_p. a) Case 3. b) Case 4. c) Case 5.

Next, the effect of adding pyrolysis modelling when enthalpy has already been included in the model is analysed by comparing cases 2 and 5. Modelling pyrolysis reactions in case 5, improves the fit of apparent c_p up to 800K (Figures 3.10b and 3.11c), reducing the fitness function (Tables 3.5 and 3.6). Regarding the baseline c_p, when modelling both enthalpy and pyrolysis reactions the optimized baseline c_p deviates considerably from the baseline c_p of TACOT (Figure 3.11c). The optimized baseline c_p is in general larger than TACOT baseline c_p except at high temperatures, when it starts to decrease. As explained previously, this behaviour makes no physical sense, so case 5 leads to a non valid baseline c_p. Thus, in this case a low fitness function indicates that the apparent c_p is accurately approximated, but not the baseline c_p.

Finally, the effect of adding enthalpy modelling when pyrolysis has already been included in the model is analysed by comparing cases 3 and 5. Modelling enthalpy in case 5 improves approximation of the apparent c_p at low temperatures (Figure 3.11c), but also increases the fitness function (Table 3.6). On the contrary, not modelling the enthalpy leads to a better fit of the apparent c_p at high temperatures and of the baseline c_p in all the temperature range under study (Figure 3.11a).

Effect of differentiating properties of char and virgin phases

Finally, char and virgin phases are considered to be different and the pyrolysis reactions are not modelled. The optimization algorithm used is the hybrid approach. Three cases are then defined, depending on whether the enthalpy is modelled or not and the model used for the properties of the char and virgin phases:

- **Case 6**. The enthalpy is not modelled. The heat capacity of the char (c_{p_c}) and virgin (c_{p_v}) phases are modelled according to equation (2.28). The total number of variables to optimize is 10: constants A_c to E_c from c_{p_c} model and constants A_v to E_v from c_{p_v} model. The subscripts "c" and "v" are used to properly identify the constants corresponding to the char and virgin phases, respectively.
- **Case 7**. The enthalpy is not modelled. The heat capacities of the char (c_{p_c}) and virgin (c_{p_v}) phases are modelled by expression (2.28) assuming that $B_c = B_v = B$, $C_c = C_v = C$ and $D_c = D_v = D$. The total number of variables to optimize is 7: constants A_c and E_c from c_{p_c} model, constants A_v and E_v from c_{p_v} model, and constants B to D from c_p models of both phases.
- **Case 8**. The enthalpies of the char (h_c) and virgin (h_v) phases are modelled by expression (2.30) taking into account that the formation enthalpy of char equals 0. Heat capacity is modelled by expression (2.28) assuming that $B_c = B_v = B$, $C_c = C_v = C$ and $D_c = D_v = D$. The total number of variables to optimize is 8: constants A_c and E_c from c_{p_c} model, constants A_v and E_v from c_{p_v} model, constants B to D from c_p models of both phases, and constant Δh_v^0 from h_v model.

Optimization results of these cases are shown in Table 3.7, in Figure 3.12 for the averaged c_p, and in Figure 3.13 for the char c_p, virgin c_p and advancement of reaction.

Table 3.7: Effect of differentiating properties of char and virgin phases: constants and fitness function.

Constant	Case 6	Case 7	Case 8
A_c	-337.12	197.57	-341.82
B_c	5029.12	-	-
C_c	-3628.55	-	-
D_c	890.99	-	-
E_c	-155.36	46.97	-14.17
A_v	-295.28	246.56	-220.49
B_v	4491.81	-	-
C_v	-3302.61	-	-
D_v	882.10	-	-
E_v	75.14	1.30	5.20
B	-	3360.84	4582.3
C	-	-2644.02	-3021.61
D	-	814.7	642.31
Δh_v^0 [J/kg]	-	-	-8.21×10^5
J	2.90	3.99	9.19

Case 1 is compared with cases 6 and 7 in order to study the effect of differentiating the properties of the char and virgin phases. Case 6 yields the lowest fitness function (Table 3.5 and Table 3.7): the optimized averaged apparent c_p and the optimized averaged baseline c_p fit accurately the dummy data in most of the temperature range, deviating slightly at low and high temperatures (Figure 3.12a). When restricting the c_{p_c} and c_{p_v} functions by sharing variables B,

C and D in case 7, both the optimized apparent c_p and the optimized baseline c_p show a more uniform discrepancy all along the temperature range, but the values are not underestimated at high temperatures (Figure 3.12b).

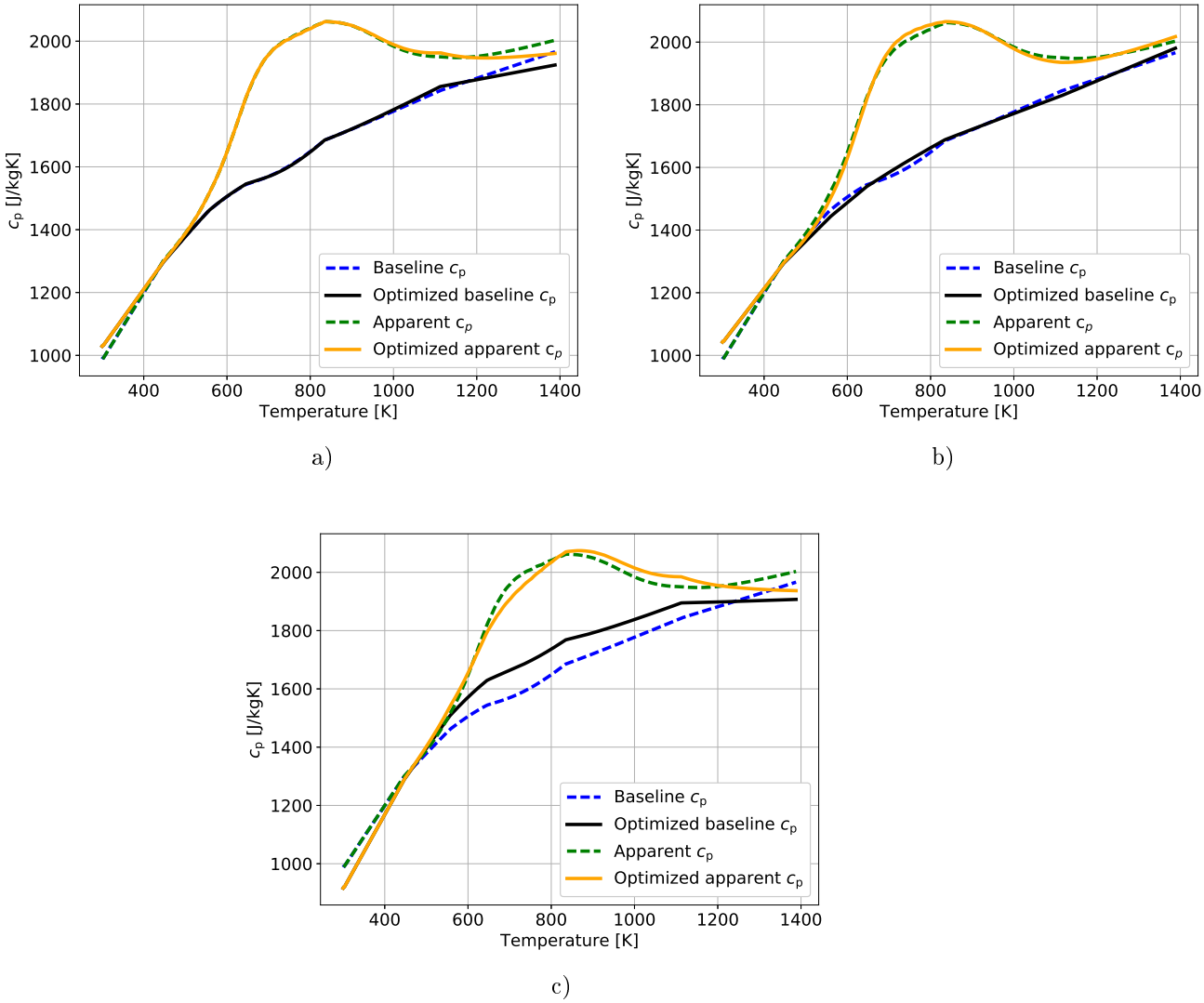

a) b)

c)

Figure 3.12: Effect of differentiating properties of char and virgin phases: averaged baseline c_p and averaged apparent c_p. a) Case 6. b) Case 7. c) Case 8.

In cases 6 and 7, the virgin phase (c_{p_v}) is properly approximated at low temperatures, but the char phase (c_{p_c}) deviates by a 50 % (Figures 3.13a and 3.13b). This is because at this temperature range the pyrolysis reaction has not started ($\chi = 0$) and there is only virgin material: the weight of the char phase in the averaged c_p (equation (3.2)) is null, so only the virgin phase plays a role in this temperature region. As χ increases the opposite happens: optimized c_{p_v} starts to deviate but optimized c_{p_c} is more accurately approximated. The virgin phase does not deviate as much as the char phase, and when the pyrolysis reaction has almost ended both phases are properly approximated. Constraining the constants B, C and D in case 7 tried to approximate c_{p_c} in a better way; however, Figure 3.13b shows that c_{p_c} is overestimated at low temperatures. In contrast, c_{p_v} is still accurately approximated: this is because when the pyrolysis reaction finishes, only 25 % of the virgin material has become char ($F = 0.25$), so the virgin phase accounts for the remaining 75 %. The algorithm can, therefore, approximate properly both phases when they are present in these percentages.

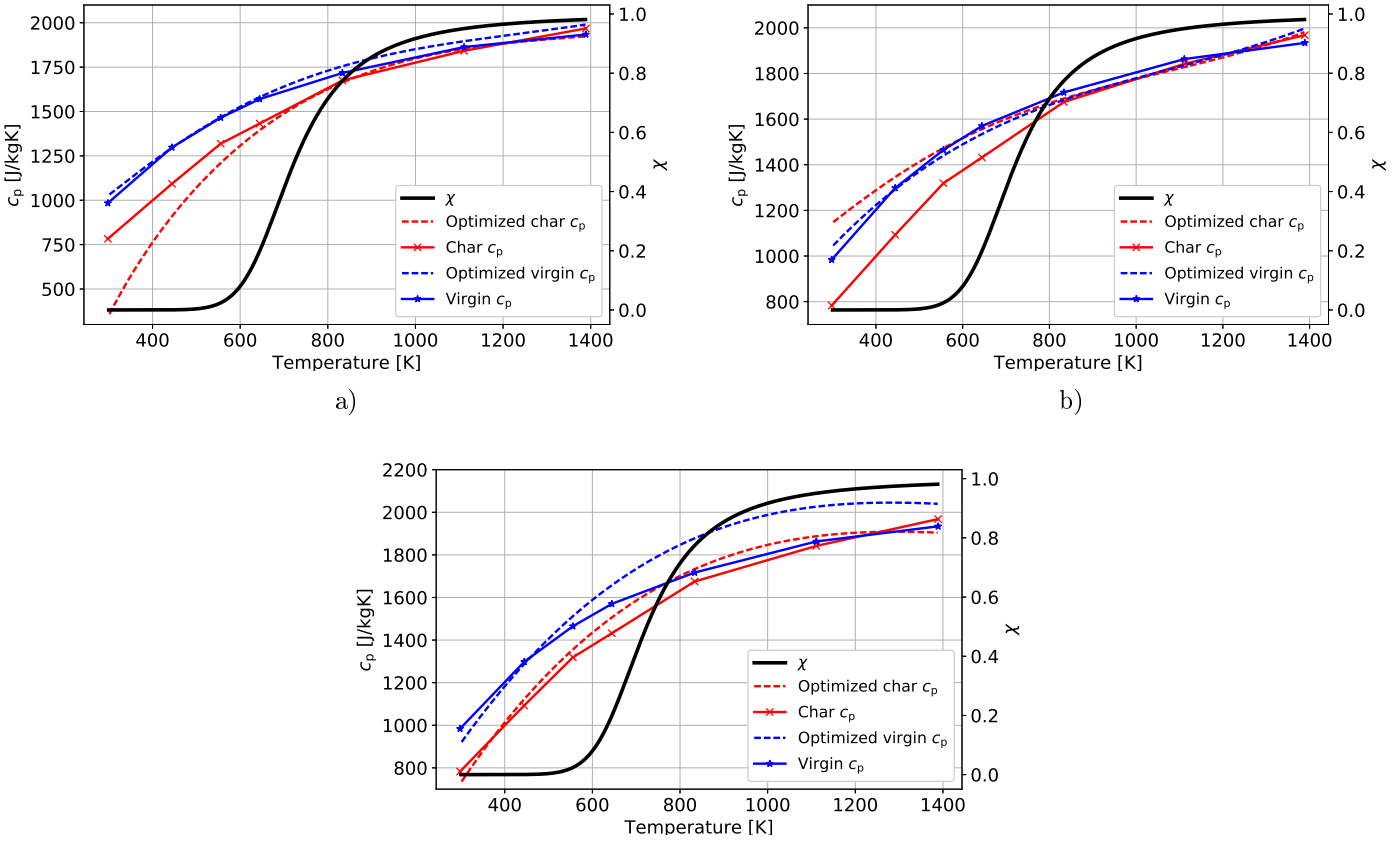

Figure 3.13: Effect of differentiating properties of char and virgin phases: char c_p and virgin c_p. a) Case 6. b) Case 7. c) Case 8.

Finally, case 7 is compared with case 8 in order to study the effect of modelling the enthalpy when the properties of the char and virgin phases are assumed to be different. Modelling the enthalpy increases the fitness function considerably, so the accuracy is lower. This is reflected in Figure 3.12c: in case 8, the optimized averaged apparent c_p and the optimized average baseline c_p deviate considerably in most of the temperature range. Furthermore, at high temperatures the optimized averaged baseline c_p starts to decrease which, as stated before, makes no physical sense. Regarding c_{p_c} and c_{p_v} for case 8, c_{p_c} is better approximated at low temperatures than in cases 6 and 7 (Figure 3.13c). However, optimized c_{p_v} deviates considerably as temperature increases. These results show that including the enthalpy when char and virgin phases are differentiated deteriorates the optimization.

From the results shown in this section, it can be concluded that modelling the char and virgin heat capacities has its limitations. In order to characterize properly char and virgin phases in a given temperature range, both phases must coexist in acceptable percentages. This is not always so: before pyrolysis starts there is only virgin material but no char, thus c_{p_c} cannot be accurately approximated. After pyrolysis, virgin material has become char, so obtaining c_{p_v} is more difficult.

Chapter 4
Conclusions

The state of the art of Thermal Protection Systems (TPS) for re-entry of space missions is focused on the development of a new series of materials known as Lightweight Ceramic Ablators (LCA). These LCA are high-porosity and low-density composite materials of carbon fibers and phenolic resin that degrade during re-entry by absorbing heat following an endothermic process known as pyrolysis. However, the proper design of TPS based on these ablative materials is limited by the fact that some of their properties, such as the specific heat capacity at constant pressure (c_p) and the enthalpy, are difficult to obtain experimentally by conventional analytical techniques (like DSC) due to coupled thermodynamic and chemical phenomena. As result, DSC experimental measurements do not provide baseline c_p data, but apparent c_p data, which also include the contributions from pyrolysis reactions. A solution to this problem can be the determination of the specific heat capacity of LCA by means of numerical simulations that implement the governing equations of the pyrolysis of these materials.

In this work, a new **numerical tool** has been developed to decouple the contributions from thermodynamics and chemistry in DSC experimental data of LCA, therefore separating the baseline c_p from the apparent c_p of these ablative materials. This numerical tool is composed of three main parts:

- **Experimental c_p data**. Experimental apparent c_p data from DSC have been modelled in this work with dummy data from the literature.
- **Pyrolysis solver for numerical c_p determination**. The OpenFOAM library, Porous Material Analysis Toolbox (PATO), has been used to obtain the numerical apparent c_p, by solving the governing equations of pyrolysis. In this work, a simplified 0D model for pyrolysis has been used for this purpose. This model needs an initial baseline c_p as input of the pyrolysis solver.
- **Optimization loop**. Optimization algorithms have been used to fit the numerical apparent c_p given by PATO to the experimental apparent c_p. The toolbox DAKOTA performs this optimization process by minimising the fitness function J, that compares the experimental apparent c_p and numerical apparent c_p. DAKOTA requires definition of the optimization algorithm (GA, gradient descent or hybrid approach), the design variables and the termination criteria.

The optimization loop changes the value of the baseline c_p that inputs the pyrolysis solver. PATO then solves the pyrolysis equations and obtains the numerical apparent c_p, which is compared to the experimental apparent c_p through the evaluation of the fitness function. This process is iterated until convergence.

Validation of this numerical tool has been performed with two reference materials of known properties: graphite and the ablative material TACOT.

Graphite was firstly used for code verification because its c_p is known and it does not undergo pyrolysis. Results show that, in general, this numerical tool can model accurately graphite c_p. Some discrepancies are however observed at low temperatures, so extrapolation of this model outside the temperature range studied here is not recommended. In addition, Uncertainty Quantification analysis confirms the suitability of this model, although being more sensitive at low and high temperatures.

TACOT was next used for code validation as an example of ablative material undergoing pyrolysis. Different cases have been analysed for TACOT optimization, in order to study the effect of taking into account different design variables in the optimization problem. First, a simple case with few variables, modelling only $c_p(T)$, was considered. Next, complexity was increased by progressively adding more variables to be modelled: enthalpy, pyrolysis reactions and properties of the char and virgin phases.

- **Effect of modelling enthalpy**. Results show that modelling enthalpy decreases optimization accuracy, by increasing the fitness function and deviation of TACOT apparent c_p.
- **Effect of modelling pyrolysis**. It has been found that optimization of the density loss during pyrolysis reduces the fitness function, thus improving approximation to TACOT baseline c_p and apparent c_p. In contrast, introducing also optimization of the advancement of reaction increases the fitness function, leading to a non-valid TACOT baseline c_p. This proves that adding more variables to the pyrolysis model reduces the accuracy of the optimization. Similarly, results show that modelling simultaneously the density loss during pyrolysis and enthalpy also decreases the optimization accuracy.
- **Effect of differentiating properties of the char and virgin phases**. Differentiating c_p of the char and virgin phases yields a good approximation of both the averaged apparent c_p and the averaged baseline c_p of TACOT. However, limitations are observed when modelling the properties of the char and virgin phases: their c_p can only be properly approximated in the temperature range where both phases coexist in acceptable percentages. On the other hand, including the enthalpy to the model increases the fitness function and leads to a less accurate approximation of both of both the averaged c_p, and the virgin c_p and char c_p.

It can therefore be concluded that this numerical tool can properly model the c_p of TACOT, by selecting adequately the input variables. In particular, the optimization accuracy can be improved when including the density loss and differentiating the properties of the char and virgin phases.

Final Conclusions

- In this work, a numerical tool based on free-license software has been successfully developed, to fit experimental c_p data of LCA through the modelling of the pyrolysis process of these materials.
- The ability of this numerical tool to separate the contributions from thermodynamics and chemistry present in experimental c_p data has been demonstrated. It has been shown that by choosing the proper design variables both the apparent c_p and baseline c_p of LCA can be accurately determined.
- Availability of accurate c_p data of LCA, like those provided by this numerical tool, can be very useful for the design of TPS based on these ablative materials.

Chapter 5
Budget

The breakdown of the costs associated to this project is shown in Table 5.1. Personnel costs have been calculated based on the scholarships that the author of this work has received: *Erasmus+ Mobility for Traineeships* and *Ministerio de Educación, Cultura y Deporte del Gobierno de España*. No costs are associated to the code development, as license-free software has been used.

The total cost of this project is **4620 €**.

Table 5.1: Personnel costs

	Hours	**Cost [€]**
Literature review	160	840
Code development	480	2520
Analysis of results	160	840
Report and presentation	80	420
Total	880	**4620**

Bibliography

[1] Adams, B. M et al. *Dakota, a multilevel parallel object-oriented framework for design optimization, parameter estimation, uncertainty quantification, and sensitivity analysis version 6.0 theory manual.* SAND2014–4253, 1177048. May 1, 2014. URL: http://www.osti.gov/servlets/purl/1177048/ (visited on 07/19/2018).

[2] Agarwal, G. and Lattimer, B. "Method for measuring the standard heat of decomposition of materials". In: *Thermochimica Acta* 545 (Oct. 2012), pp. 34–47. ISSN: 00406031. URL: http://linkinghub.elsevier.com/retrieve/pii/S0040603112003139 (visited on 07/16/2018).

[3] Anderson Jr., J. D. *Hypersonic and High-Temperature Gas Dynamics.* Second. Reston ,VA: American Institute of Aeronautics and Astronautics, Jan. 2006. ISBN: 978-1-56347-780-5 978-1-60086-195-6.

[4] Bellas-Chatzigeorgis, G. "Development of Advanced Gas-Surface Interaction Models for Chemically Reacting Flows for Re-Entry Conditions". PhD thesis. Milan, Italy: Politecnico di Milano, Feb. 2018. 161 pp.

[5] Box, G. E. P. and Tiao, G. C. *Bayesian Inference in statistical analysis.* Addison-Wesley series in behavioral science. Reading, Mass.: Addison-Wesley, 1973. 588 pp. ISBN: 978-0-201-00622-3.

[6] Coheur, J. et al. "Uncertainty Quantification of Aerothermal Flow-Material Simulations of Low-Density Ablative Thermal Protection Materials". In: *8th VKI PhD Symposium* ().

[7] Conley, J. L. and Peterson, K. H. "What are the origins of Thermal Protection Systems?" Georgia Institute of Technology. Atlanta, United States of America., Apr. 4, 2011. URL: https://ntrs.nasa.gov/search.jsp?R=20110023700 (visited on 06/08/2018).

[8] Daw, J. E. *Measurement of Specific Heat Capacity Using Differential Scanning Calorimeter.* INL/EXT-08-15056, 941744. Nov. 1, 2008. URL: http://www.osti.gov/servlets/purl/941744-Mhj2hs/ (visited on 03/19/2018).

[9] Duffa, G. *Ablative Thermal Protection Systems Modeling.* Washington, DC: American Institute of Aeronautics and Astronautics, Inc., May 2013. ISBN: 978-1-62410-171-7.

[10] Goddard, R. H. *Report Concerning Further Development.* Mar. 1920. URL: https://siarchives.si.edu/history/featured-topics/stories/march-1920-report-concerning-further-developments-space-travel (visited on 04/02/2018).

[11] Goldberg, D. E. *Genetic Algorithms in Search, Optimization and Machine Learning.* 1st. Addison-Wesley series in behavioral science. Boston, USA, 1989.

[12] Helber, B. "Material Response Characterization of Low-density Ablators in Atmospheric Entry Plasmas". PhD thesis. Brussels, Belgium: Vrije Universiteit Brussel, Jan. 2016. 251 pp.

[13] ISO 11357-4:2014. *Plastics – Differential scanning calorimetry (DSC) – Part 4: Determination of specific heat capacity.* 2014.

[14] Lachaud, J. and Mansour, N. N. "Porous-Material Analysis Toolbox Based on OpenFOAM and Applications". In: *Journal of Thermophysics and Heat Transfer* 28.2 (Apr. 2014), pp. 191–202. ISSN: 0887-8722, 1533-6808.

[15] Lachaud, J. et al. "A generic local thermal equilibrium model for porous reactive materials submitted to high temperatures". In: *International Journal of Heat and Mass Transfer* 108 (May 2017), pp. 1406–1417. ISSN: 00179310.

[16] Lachaud, J. et al. "Ablation Workshop Test Case". In: *4th Ablation Workshop* (Mar. 2011), p. 4.

[17] Laub, B. and Venkatapathy, E. "Thermal protection system technology and facility needs for demanding future planetary missions". In: 544 (Jan. 2004), pp. 239–247.

[18] Mooij, E. *AE4870B - Re-entry systems Lecture Notes*. Technische Universiteit Delft Course. Faculty of Aerospace Engineering, TU Delft. Delft, Netherlands, 2017. 507 pp.

[19] NASA. *Launch of Apollo 11*. URL: `https://www.nasa.gov/content/launch-of-apollo-11` (visited on 06/04/2018).

[20] Nocedal, J. and Wright, S. J. *Numerical optimization*. 2nd ed. Springer series in operations research. New York: Springer, 2006. 664 pp. ISBN: 978-0-387-30303-1.

[21] Park, W. C., Atreya, A., and Baum, H. R. "Experimental and theoretical investigation of heat and mass transfer processes during wood pyrolysis". In: *Combustion and Flame* 157.3 (Mar. 2010), pp. 481–494. ISSN: 00102180. URL: `http://linkinghub.elsevier.com/retrieve/pii/S0010218009002843` (visited on 03/22/2018).

[22] POCO graphite. *Properties and characteristics of graphite*.

[23] Privault, N. *Understanding Markov chains: examples and applications*. Springer undergraduate mathematics series. Singapore: Springer, 2013. 354 pp. ISBN: 978-981-4451-50-5.

[24] Querin, O. M. *CIVE5024 Design Optimization Course Lecture Notes*. University of Leeds Course. School of Mechanical Engineering, University of Leeds. Leeds, United Kingdom., 2016. 188 pp.

[25] Raitt, D. and Edwards, B. "The Space Elevator: Economics and Applications". In: *th International Astronautical Congress*. 55th International Astronautical Congress (2004), p. 13.

[26] Ribes Greus, A., Vilaplana Domingo, F., and Contat Rodrigo, L. *Thermal Characterisation of Polymeric Materials*.

[27] Riccio, A. et al. "Three-dimensional modeling of composites fire behavior". In: *Journal of Reinforced Plastics and Composites* 33.7 (Apr. 2014), pp. 619–629. ISSN: 0731-6844, 1530-7964. URL: `http://journals.sagepub.com/doi/10.1177/0731684413512226` (visited on 05/21/2018).

[28] Rubinstein, R. Y. and Kroese, D. P. *Simulation and the Monte Carlo Method*. Second. Wiley-Interscience. 377 pp.

[29] Science Museum London. *Silica Space Shuttle thermal protection (TPS) tile*. 1980. URL: `https://www.scienceandsociety.co.uk/results.asp?image=10309930&itemw=4&itemf=0001&itemstep=161&itemx=216` (visited on 03/25/2018).

[30] *Specific heat according DIN 51007*, p. 6.

[31] Torres Herrador, F. J. "Experimental Characterization and Simulation of Pyrolysis Phenomenon: from Carbon Composite Ablators to Pacific Islands Plant Biomass". Master Thesis. Rhode-Saint-Genèse, Belgium: von Karman Institute for Fluid Dynamics, June 2017. 103 pp.

[32] Torres Herrador, J. F. "Thermal Characterization of Ablative Materials". Master Thesis. Valencia, Spain: Universitat Politècnica de València, July 2016. 101 pp.

[33] Tran, H. K. *Development of Lightweight Ceramic Ablators and Arc-Jet Test Results*. Technical Memorandum. Moffet Field, California, USA: NASA Ames Research Center., Jan. 1994, p. 28.

[34] Trick, K.A., Saliba, T.E., and Sandhu, S.S. "A kinetic model of the pyrolysis of phenolic resin in a carbon/phenolic composite". In: *Carbon* 35.3 (1997), pp. 393–401. ISSN: 00086223. DOI: 10.1016/S0008-6223(97)89610-8. URL: http://linkinghub.elsevier.com/retrieve/pii/S0008622397896108 (visited on 04/15/2018).

[35] Wong, H. et al. "Detailed analysis of species production from the pyrolysis of the Phenolic Impregnated Carbon Ablator". In: *Journal of Analytical and Applied Pyrolysis* 122 (Nov. 2016), pp. 258–267. ISSN: 01652370. URL: http://linkinghub.elsevier.com/retrieve/pii/S016523701630211X (visited on 02/25/2018).

[36] Yuriesfera. *La misión: El vuelo de Gagarin*. URL: https://yuriesfera.net/documentos/la-mision/ (visited on 06/04/2018).